MLM--3072

DE83 014260

MLM-3072
UC-4 and UC-22

Mound Activities in Chemical and Physical Research: July-December 1982

Issued: June 20, 1983

MOUND
Miamisburg, Ohio 45342

operated by
MONSANTO RESEARCH CORPORATION
a subsidiary of Monsanto Company

for the
U. S. DEPARTMENT OF ENERGY

Contract No. DE-AC04-76-DP00053

Foreword

This report is issued semiannually by Mound. Under the sponsorship of the DOE Division of Basic Energy Sciences, Mound is responsible for research in the physical sciences to further the progress of science and technology in the public interest. This report is submitted by B. R. Kokenge, Director of Nuclear Operations, and R. E. Vallee, Manager of Technology Applications and Development, from contributions prepared by W. M. Rutherford, Science Fellow (Thermal Diffusion) W. L. Taylor, Science Fellow (Gas Dynamics and Cryogenics); G. L. Silver, Science Fellow (Separation Chemistry); C. J. Wiedenheft, Leader, Metal Hydride Research; and from members of the Isotope Separation Section: W. R. Wilkes, Isotope Separation Manager; E. D. Michaels, Leader, Isotope Separation Research and Development.

These reports are not intended to constitute publication in any sense of the word. Final results either will be submitted for publication in regular professional journals or will be published in the form of MLM topical reports.

Previous reports in this series are:

MLM-2296	MLM-2654
MLM-2354	MLM-2727
MLM-2414	MLM-2756
MLM-2450	MLM-2809
MLM-2506	MLM-2884
MLM-2555	MLM-2892
MLM-2590	MLM-2998

Contents

I. Low temperature research

II. Separation research

I. Low temperature research

Reaction rates of deuterium-tritium mixtures

G. T. McConville, D. A. Menke
and R. E. Ellefson

The reaction rate experiments for the formation of DT in D_2+T_2 mixtures have been extended to lower temperatures. The observations produced a surprise, and they continue to indicate that the reaction process is exceedingly complex. The pressure dependence of the reaction at constant initial T_2 concentration, the dependence of the reaction on initial T_2 concentration, and the effect of CT_4 and T_2O impurities were presented in the last progress report [1].

The temperature dependence of the reaction rate at a pressure of 300 torr for an initial T_2 concentration of 30% is shown in Figure I-1. The triangles (▲) represent experiments where there were no measured impurities. The initial T_2 had a CT_4 content of less than 10 ppm as determined with a gas chromatograph. The mass spectrometer determination at the time of the experiment had a lower limit of 30 ppm. These data confirm the initial, very fast experiment at 195 K. Between 230 K and 160 K, the scatter in the data indicate that the reaction rate is being limited by undetected impurities. The measurements made with the order of 120 ppm CT_4 in the T_2 indicated by the circles (●) show that the presence of CT_4 nearly eliminates the fast reaction times. Figure I-1 shows a hint of the peak as one approaches 195 K. Measurements below 195 K with CT_4 present will show whether the peak has been shifted to lower temperatures.

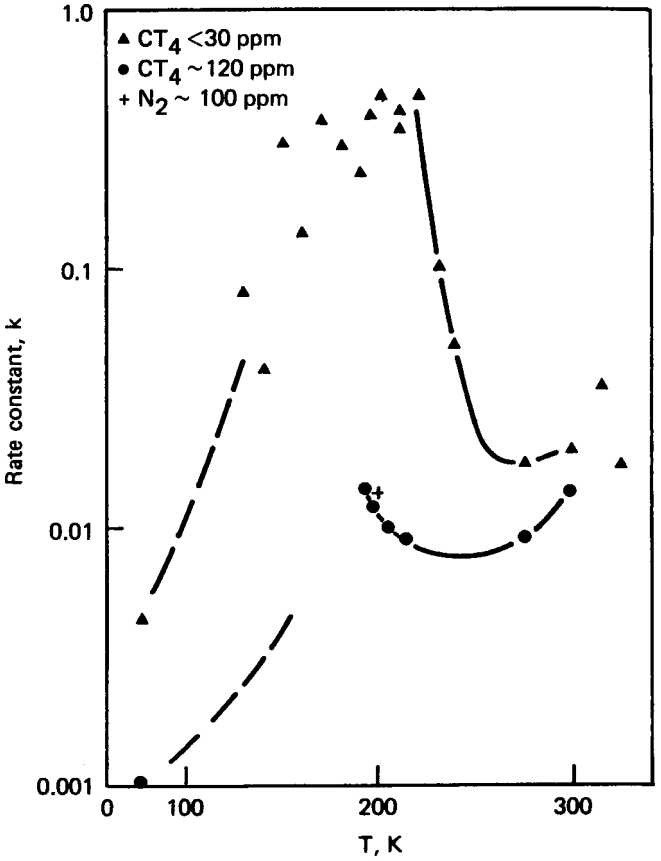

FIGURE I-1 - Temperature dependence of D_2+T_2 to produce DT for three different impurity contents.

If one uses the argument, given in the last progress report, that ln2/k is linear in CT_4 content during the reaction, the difference in the very fast reactions (represented by the scatter) near 200 K represents differences in CT_4 concentrations of only a few parts per million. Measurements of the concentration dependence of CT_4 on the reaction rate k need to be made to confirm that the linear dependence seen at 295 K can be used to describe the effect at 195 K. The shape of the temperature dependence of the reaction rate for the pure T_2 and D_2 indicates that the mechanism for the reaction is quite complex.

The argument of Schaeffer and Thompson [2] is that the reaction proceeds by an ion-molecule chain. The fast electron from the tritium decay produces T_3^+ through the reactions

$$e^- + T_2 \rightarrow T_2^+ + 2e^- \quad (1)$$

and

$$T_2^+ + T_2 \rightarrow T_3^+ + T. \quad (2)$$

The T_3^+ can then form a chain by interacting with a D_2, passing on the charge and forming DT

$$T_3^+ + D_2 \rightarrow T_2D^+ + DT. \quad (3)$$

The chain lasts as long as the charge is passed to a species that can produce DT. If CT_4 is present,

$$CT_4 + T_3^+ \rightarrow CT_5^+ + T_2 \quad (4)$$

and the CT_5^+ stops the chain. A second way CT_4 could affect the reaction is to reduce the amount of T_3^+ present at the start of the DT reaction by competing for the charge by forming CT_5^+.

Looking at Figure I-1, the point represented by the (+) has nearly the same reaction time as the mixture containing 120 ppm CT_4. But, in this case, the impurity was N_2 in the D_2 and not the T_2. This observation may indicate that it is the charge transfer after the D_2 has been mixed with T_2 that controls the reaction rate. It will be shown that, with CT_4 present in the initial T_2 the T_3^+ concentration depends on reaction rates that are not well known. Assuming the reaction cross section for $T_3^+ + T^- \rightarrow 2T_2$ and $CT_5^+ + T^- \rightarrow CT_4 + T_2$ are about the same, the presence of CT_4 does not change the T_3^+ concentration enough to cause the reductions in rate constant k seen in Figure I-1.

In collaboration with J. T. Gill, a simple reaction model has been devised which appears to describe the dependence of k on the initial T_2 concentration at 295 K when CT_4 is present. The model only assumes ground state molecule-ion interactions, and this may be the reason the model does not describe the dependence of k on the initial T_2 concentration in the absence of CT_4. One can define a reactant ion R as one of the following, T_3^+, T_2D^+, TD_2^+, or D_3^+ formed by the interaction of fast electrons with D_2 and T_2 with a rate K_r. Thus,

$$\beta + T_2 \xrightarrow{K_r} R_T \qquad R_T = \frac{T_2}{D_2+T_2}R \quad (5)$$

or

$$\beta + D_2 \xrightarrow{K_r} R_D \qquad R_D = \frac{D_2}{D_2+T_2}R \quad (6)$$

and

$$R_T + D_2 \xrightarrow{K_s} DT \quad (7)$$

or

$$R_D + T_2 \xrightarrow{K_s} DT \quad (8)$$

and

$$R + CT_4 \xrightarrow{K_q} CT_5^+. \quad (9)$$

Then

$$\frac{d(DT)}{dt} = K_sD_2R_T + K_sT_2R_D = 2\,\frac{K_sT_2D_2R}{T_2+D_2}. \quad (10)$$

One obtains R from the steady state equation,

$$0 = \frac{dR}{dt} = K_r \beta (D_2+T_2) - \frac{2K_s T_2 D_2 R}{D_2+T_2} - K_q R C T_4 \quad (11)$$

giving

$$R = \frac{K_r \beta [D_2+T_2]}{2K_s \frac{D_2 T_2}{T_2+D_2} + K_q C T_4} \quad (12)$$

Let K_β represent the production of electrons from the change of T_2 to He_3^+. Then the concentration of electrons, β, is

$$K_\beta T_2 - [D_2+T_2] K_r = 0 \quad (13)$$

Substituting (13) in (12) and then (12) in (10),

$$\frac{d[DT]}{dt} = \frac{2K_\beta K_r D_2 (T_2)^2/(D_2+T_2)}{2K_s \frac{D_2 T_2}{(D_2+T_2)} + K_q C T_4} \quad (14)$$

The yield of the reaction is the rate of production of DT per T_2 disintegration.

$$G = \frac{\frac{d[DT]}{dt}}{K_\beta T_2} \quad (15)$$

In the case where CT_4 is present and $K_q CT_4 >> 2K_s D_2 T_2/(T_2+D_2)$, the yield is G = constant x $T_2 D_2$, whereas in the case of CT_4 below detection limit, G = constant. In Figure I-2, we reproduce the yield as a function of initial T_2 concentrations from the 295 K. The circles represent data with CT_4 present and show a $T_2(1-T_2)$ dependence, whereas the triangles and squares represent data with

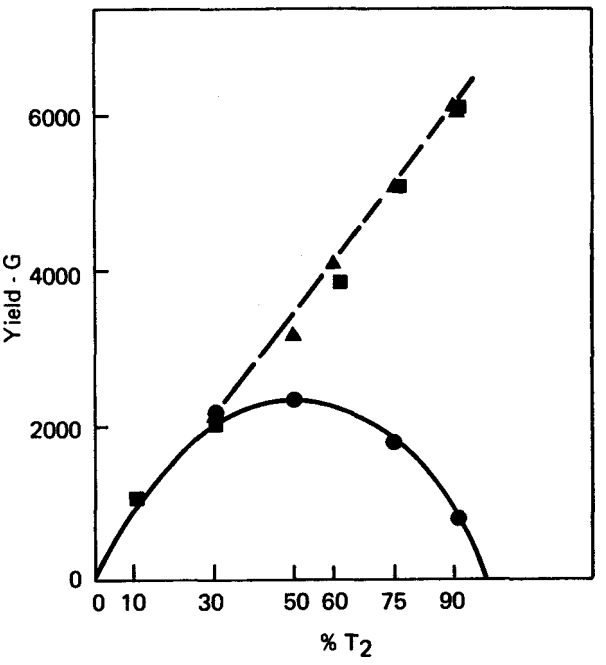

FIGURE I-2 - Reaction rate yield as a function of initial T_2 concentration in two limiting cases; ▲ and ■, no detectable CT_4 impurity, and ●, CT_4 = 120 ppm.

less than 10 ppm CT_4 present displaying a linear increase in G which is at odds with the model prediction of G = constant. In our last report [1], we showed that the observation of Souers et al [3] of $T^- >> e^-$ is consistent with a large excited state T_2^* in the pure T_2. Addition of excited state molecules to the above model is the next step in trying to explain the data.

Calculation of charged particle densities in tritium containing CT_4 impurity

G. T. McConville

In our last report [1], a calculation of the charged particle densities in pure tritium gas was described. It was shown that tritium is not just a combination of T_2 molecules and a few decay electrons. The energy from the electrons is distributed in the gas, producing, in addition to ground state

T_2 molecules, the following: T_2^* (excited states), T_2^+, T_3^+, T^- and β^- or e^-. We take β^- to be hot electrons and e^- to be thermal electrons. Eight reaction equations were given from which the steady state concentrations of the ions were obtained. It was shown that, to obtain the ratio of T^- to e^- observed by Souers et al [3], a T_2^* concentration of the order of 10^{15} per cm^3 was necessary.

When one adds CT_4 to the T_2 mixture, the most probable additional reactions are the following:

$$T_3^+ + CT_4 \rightarrow CT_5^+ + T_2 \qquad (1)$$

$$CT_5^+ + T^- \rightarrow CT_4 + T_2 \qquad (2)$$

$$CT_5^+ + e_3^- \rightarrow CT_4 + T \qquad (3)$$

In the absence of measured cross sections, they can be inferred from reactions given in Table I-5 in the previous report [1] and from the chain reaction

$$T_3^+ + D_2 \rightarrow T_2D^+ + DT \qquad (4)$$

for which values of the reaction constant, k, are known (to within a factor of $\sqrt{2}$). We make the assumption that the effect of CT_4 in Equation 1 is the same as D_2 in Equation 4. Thus, for Equation 1, the reaction rate is $k_9 = 12^{-12}$. The effect of CT_5^+ in Equations 2 and 3 is the same as T_3^+ in the fourth and sixth equations of Table I-5 in reference 1. Thus, for Equation 2, $k_{10} = k_4 = 5 \times 10^{-9}$ and for Equation 3, $k_{10} = k_{11} = k_6 = 5 \times 10^{-8}$.

The steady state equations obtained by combining the equations in Table I-5 of reference 1 with Equations 1, 2, and 3 are:

$$T_2^+ T_2 k_2 = ne_1^- T_2 k_1 + e_3^- T_3^+ k_5 \qquad (5)$$

$$T_3^+ = \frac{T_2 + T_2 k_2}{e_3^-(k_4 + k_5) + T^- k_6 + CT_4 k_9} = \frac{ne_1 T_2 k_1}{e_3^- k_4 + T^- k_6 + CT_4 k_9} \qquad (6)$$

$$CT_5^+ = \frac{T_3^+ CT_4 k_9}{T^- k_{10} + e_3^- k_{11}} \qquad (7)$$

$$e_3^- = \frac{2ne_1 T_2 k_1}{T_2 k_3 + T_3^+(k_4+k_5) + CT_5^+ k_{11} + T_2^* k_8} \qquad (8)$$

$$T^- = \frac{T_3^+ e_3^- + T_2 e_3^- k_3 + e_3^- T_2^* k_8}{e_3^- k_4 + T^- k_6 + CT_4^- k_{10}} \qquad (9)$$

Using the values of ne_1, T_2, and k_1 from reference 1, $ne_1 T_2 k_1 = 6 \times 10^{26}$. Then letting $T_2^* k_8 = A$ and $CT_4 k_9 = B$, and letting the unit of the ion concentrations be 10^{13} particles, Equations 6 through 9 become:

$$T_3^+ = \frac{6}{0.5\, e_3^- + 5T^- + B} \qquad (10)$$

$$CT_5^+ = \frac{T_3^+ B}{4T^- + 0.6e^-} \qquad (11)$$

$$e_3^- = \frac{6}{2.3T_3^+ + 4CT_5^+ + A} \qquad (12)$$

$$T^- = \frac{e_3^- T_3^+ + e_3^- A}{5T_3^+ + 4CT_5^+}. \qquad (13)$$

Thus, A is a measure of the excited state T_2 molecules and B a measure of the CT_4 impurity. It turns out these four equations are not independent, and one must also include the charge equality equation,

$$T_3^+ + CT_5^+ = T^- + e_3^- \qquad (14)$$

Solving these equations with $k_9 = 10^{-12}$ and $CT_4 = 10^{-4}$ T_2 (0.01% concentration) and assuming $T_2^* = 0$, we obtain $e_3^- = 0.058$, $T^- = 1.06$, $T_3^+ = 0.94$, and $CT_5^+ = 0.18$. If there were no CT_4 present, then $T_3^+ = 1.1$, and we see that the introduction of CT_4 does not reduce the T_3^+ concentration much. It also can be seen from Equations 10 through 13 that increasing T_2^* affects e_3^- and T^- as in reference 1, but has no effect on T_3^+ because there is no cross term involving T_2^* and T_3^+ in any of the equations. Increasing T_2^* to 5×10^{-5}, T_2 decreases e_3^- to 0.01 (in units of 10^{-13} particles). Increasing either CT_4 or k_9 an order of magnitude in Equations 10 and 11 does invert the T_3^+ and CT_5^+ populations, giving $T_3^+ = 0.39$ and $CT_5^+ = 0.71$. Increasing B another order of magnitude produces $T_3^+ = 0.06$ and $CT_5^+ = 1.09$. Thus, increasing either the CT_4 concentration or the reaction rate, k_9, for the production CT_5^+, could reduce the rate of production of DT by reducing the initial T_3^+ concentration. The experimental observation that 100 ppm N_2 in the D_2 before mixing has about the same effect in reducing k (shown in Figure I-1) as 120 ppm CT_4 in the T_2 leads one to think the assumed value of $k_9 = 10^{-12}$ is about right. To confirm this idea, we must find a published value of k_9 or find an independent way of determining the relative effect of either CT_4 or N_2 replacing D_2 in Equation 4.

Deuterium triple point fixed temperature

G. T. McConville

As a result of the publication of high quality deuterium vapor pressure measurements [4,5], we have engaged in a cooperative program with Franco Pavese of the Institute of Metrology "G. Colonnetti" in Turin, Italy, to examine the possibility of introducing the triple point of well characterized D_2 as a fixed point for the 1985-1986 revision of the International Practical Temperature Scale (IPTS). The determination of the fixed point temperatures with gas thermometry is becoming so good that thought is being given to removing boiling points as fixed points. The low temperature end of the IPTS is at 13.81 K because an interpolating instrument for lower temperatures has not been agreed to by the National Standards Laboratories. Down to 13.81 K the standard platinum resistance thermometer is the interpolating instrument. The germanium resistance thermometer has been considered as a lower temperature interpolating instrument. As can be seen in Figure I-3, the interpolating function for either instrument is complicated. Because of the curvature of the temperature dependence of the platinum resistor below 20 K, an additional fixed point was desirable near 17 K. The figure shows the neon triple point (T = 24.55 K), eH_2 boiling point (T = 20.28 K) and the eH_2 triple point (T = 18.81 K). The additional point eH_2(25) is the temperature of eH_2 at a vapor pressure of 25 cm-Hg (T = 17.04 K).

The proposal is to replace the two eH_2 points with the eD_2(TP) point (T = 18.73 K). Several Standards Laboratories have made D_2 triple point measurements [6] which

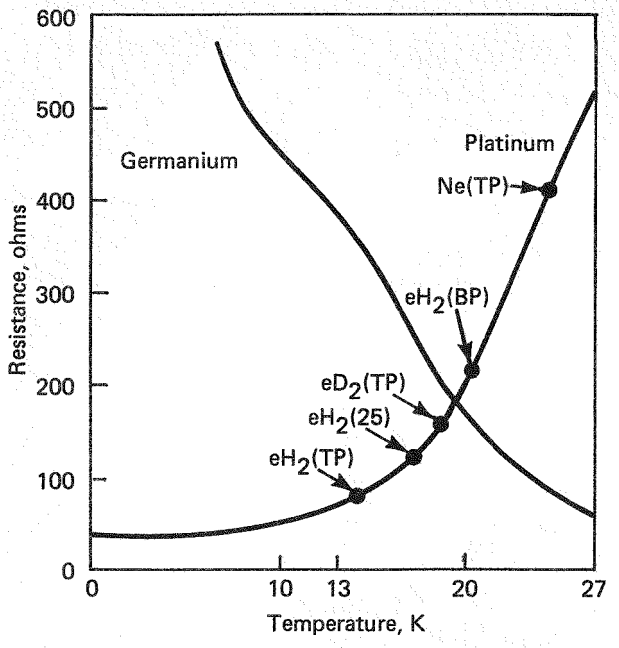

FIGURE I-3 - Temperature dependence of platinum and germanium thermometers with fixed point temperatures represented on the platinum thermometer curve.

disagree by the order of 0.03 K. We were able to show that the most likely reason for the difference was a difference in the HD concentration [5] in the different D_2 samples. The HD concentration can be reduced by using isotopically purified D_2 and specially conditioning the container as is done in tritium service. We have obtained specially constructed triple point cells from Quantum Mechanics, Inc., which have been conditioned to be ultra clean and to have virtually no protium ingrowth (Figure I-4). The cells will be filled with Mound D_2 which presently tests <30 ppm HD in the separating column.

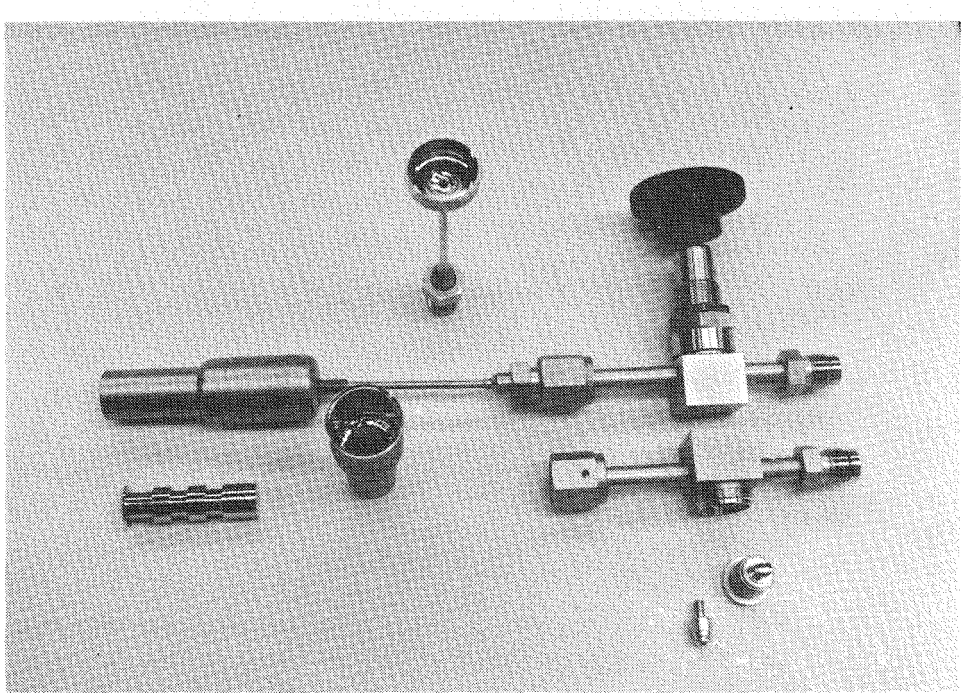

FIGURE I-4 - Specially treated D_2 triple point cells built by Quantum Mechanics, Inc.

II. Separation research

Liquid phase thermal diffusion

W. M. Rutherford

THERMAL DIFFUSION OF METHYL CHLORIDE

Isotopic separation experiments with methyl chloride were described in a previous report [1]. To interpret these data in terms of the theory of the thermal diffusion column, it is necessary to have accurate values of the physical properties of the fluid as a function of temperature. In general, requisite property data are incomplete or do not exist in the temperature range of interest (20°C - 160°C). A 1977 report [2] described a preliminary effort to estimate viscosity, diffusion, and thermal conductivity coefficients for methyl chloride. Subsequently, a high pressure viscometer was constructed and used to measure the viscosity of methyl chloride as a function of temperature and pressure [3]. The availability of this new data led to a reassessment of the earlier estimates of the diffusion and thermal conductivity coefficients and to a more reliable interpretation of the column separation measurements.

DIFFUSION

The diffusion coefficient for methyl chloride was estimated based on a corresponding states correlation developed by Dawson, Khoury and Kobayashi [4]. Thus:

$$\rho D = (\rho D)_o \, (1 + b\rho_r + c\rho_r^2 + d\rho_r^3) \qquad (1)$$

where:

- D = diffusion coefficient
- ρ = density
- ρ_r = reduced density
- b = 0.053432
- c = -0.030182
- d = -0.029725

The subscript o denotes the value for the dilute gas as evaluated from the kinetic theory.

THERMAL CONDUCTIVITY

The corresponding states technique used for the first estimate [2] of thermal conductivity was reworked and improved. The thermal conductivity was calculated according to

$$\lambda = \lambda_o \beta \, (T_R, P_R, \omega) \qquad (2)$$

where

- λ = thermal conductivity
- T_R = reduced temperature
- P_R = reduced pressure
- ω = Pitzer acentric factor

λ_o is the thermal conductivity at an arbitrarily chosen reference point, $T_R = 0.7$ and $P_R = 1$. Data for six compounds in the Jamieson, Irving and Tudhope compilation [5] were interpolated to $P_R = 1.873$, which is equivalent to the operating pressure of 123.5 atm used for the column experiments. A second interpolation to $\omega = 0.156$ yielded a relationship between β and the reduced temperature for methyl chloride. This, combined with a value of λ_o estimated from the TPRC Tables [6], yielded the thermal conductivity as a function of temperature.

COLUMN COEFFICIENTS

Experimental separation data for the $CH_3{}^{35}Cl$ - $CH_3{}^{37}Cl$ pair had been acquired in the 45-cm research column at hot to cold wall spacings of 258 μm and 208 μm [1]. The data from these experiments have now been reevaluated in terms of the new property values given in Table II-1. Results of the calculation are reported

Table II-1 - PHYSICAL PROPERTIES OF METHYL CHLORIDE AT 123.5 atm

t (°C)	Density (g/cm^3)	Viscosity (cP)	Diffusion Coefficient $cm^2/sec \times 10^5$	Conductivity $cal/sec/cm/K \times 10^4$
20	0.943	0.200	6.19	4.03
40	0.907	0.169	8.02	3.75
60	0.868	0.143	10.19	3.46
80	0.827	0.122	12.66	3.19
100	0.781	0.104	15.68	2.92
120	0.728	0.0880	19.37	2.66
140	0.667	0.0720	24.21	2.40
160	0.585	0.0562	31.40	2.17

in Tables II-2 and II-3. The quantities reported are defined by

H_{ij} = initial transport coefficient for the ij^{th} pair

K = remixing coefficient

α_T = isotopic thermal diffusion factor at the average temperature

α_o = reduced isotopic thermal diffusion factor defined by

$$\alpha_o = \alpha_T (m_i + m_j)/m_i - m_j)$$

m_i, m_j = molecular weights

The agreement between measured and calculated values of K is a sensitive test of the theoretical description of the performance of the column. The current set of calculations shows very satisfactory agreement at the 254 μm spacing. This is a strong indication that the derived values of α_T and α_o are reliable. The larger discrepancy in K at the 203 μm spacing is probably the result of small parasitic effects which are quite likely to be encountered at smaller gaps.

Table II-2 - DIMENSIONS AND OPERATING CONDITIONS FOR LIQUID PHASE THERMAL DIFFUSION EXPERIMENTS WITH METHYL CHLORIDE

	Experiment A	Experiment B
Spacing, μm	258	208
Cold wall diameter, cm	1.9286	1.9286
Length, cm	45.56	45.56
Hot wall temperature, °C	154.8	153.1
Cold wall temperature, °C	50.59	56.22
Pressure, atm	123.5	123.5

Table II-3 - COLUMN PARAMETERS FOR LIQUID PHASE THERMAL DIFFUSION EXPERIMENTS WITH METHYL CHLORIDE

	Theory	Experiment
Experiment A		
10^5H g/sec	-	24.91
K, g cm/sec	0.0384	0.0362
α_T	-	0.0328
α_o	-	1.68
Experiment B		
10^5H g/sec	11.39[a]	12.15
K, g cm/sec	0.00742	0.00825

[a]Based on value of α_T calculated from measured H value of Experiment A.

SEPARATION OF BROMINE-81

A previous report described the separation of ^{79}Br by liquid phase thermal diffusion of bromobenzene in the 13-column experimental cascade [3]. Following the completion of that campaign, the experimental cascade was enlarged to 14 columns and prepared for the separation of ^{81}Br. The cascade, as currently configured, has a 740-g feed reservoir at the top and a 16-g product reservoir one stage up from the bottom. The bottom stage, a small, 30-cm column, is used to accumulate heavy impurities. The cascade is operated in the batch mode.

The ^{81}Br campaign was started on May 5, and its progress toward the desired goal of 90 percent enrichment is depicted in Figure II-1. There is a hiatus in the plot which represents 60 days lost as the result of a leak and of several interruptions of the steam supply to the cascade.

The ^{81}Br separation is somewhat more difficult than the ^{79}Br separation, although the natural abundances of both isotopes are approximately the same. There is a significant interference from the singly and doubly substituted ^{13}C bromobenzene species. These tend to transport ^{79}Br to the bottom of the system thereby reducing the ^{81}Br enrichment. This effect, however, has been taken into account in calculating the theoretical curve of Figure II-1. We cannot at present explain the decline in performance relative to theory in the later stages of the separation. This phenomenon has been observed in previous experiments.

Calcium isotope separation

W. M. Rutherford

Previous reports [7,8] have described a process for separating calcium isotopes by liquid phase thermal diffusion of an aqueous calcium nitrate solution. A technique was developed for selectively suppressing the separation of the calcium salt from the water. The concept involves setting up a net flow of water through the apparatus at a rate just sufficient to counteract separation of the solute from the solvent. According to theory previously developed [9], the separation of the isotopes is not affected by the solvent counterflow.

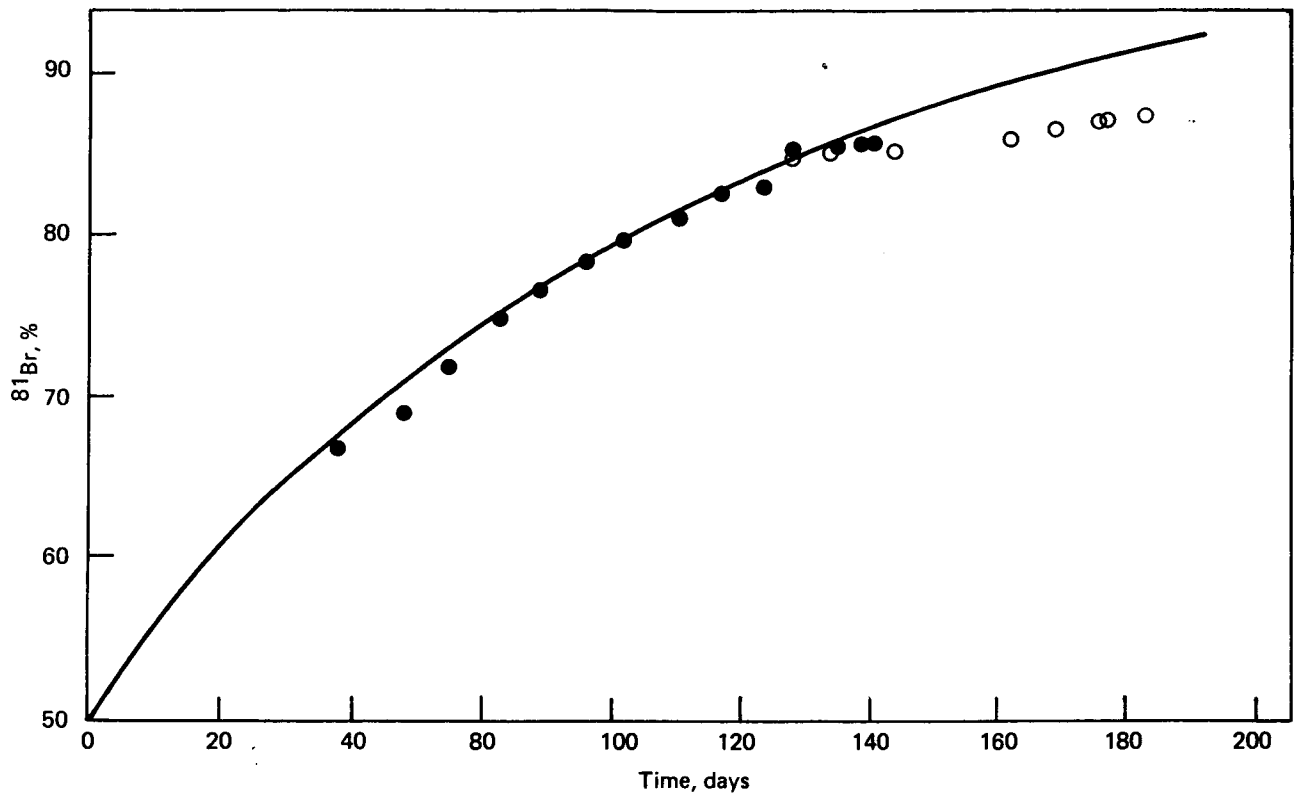

FIGURE II-1 - Separation of ^{81}Br by liquid phase thermal diffusion of bromobenzene in a 14-column cascade. The open circles are shifted to the left by 60 days, to account for system interruptions.

In the last report, we described the results of several counterflow experiments in columns 114 and 15-cm long. The experiments had three objectives. These were: 1) to determine the initial transport rate for the solute-solvent pair in order to establish the criterion for setting the solvent counterflow rate, 2) to determine the steady-state separation of the ^{40}Ca-^{48}Ca pair, and 3) to determine the initial transport rate for the isotopic separation.

The previous results have now been augmented by results from two additional experiments with the 15-cm column. In addition, we carried out a systematic series of transient experiments to determine the solute-solvent transport rate in the 114-cm column as a function of concentration.

Isotopic separations observed at the steady-state for all of the recent experiments are given in Table II-4, along with the solute concentrations at the top and bottom of the column. These data are the composite of a number of measurements taken during each experiment over periods of several weeks of continuous stable operation.

The symbol, q, in Table II-4 refers to the isotopic separation factor for the ^{40}Ca-^{48}Ca pair. The isotopic separation factor is defined by:

$$q = R_B/R_T \qquad (1)$$

where R_B is the ratio of ^{48}Ca to ^{40}Ca at the bottom of the column, and R_T is the similar ratio at the top.

Table II-4 - SEPARATION OF CALCIUM ISOTOPES BY LIQUID PHASE THERMAL DIFFUSION

Experiment	Column Length (cm)	Solute Concentration (wt %) Top	Bottom	Isotopic Separation Factor (q)
L3	114	4.13	12.99	1.647
L4	114	24.71	31.69	1.293
S1	15	36.87	41.80	1.240
S2	15	3.94	6.68	1.236
S3	15	35.46	40.06	1.195

According to theory, the natural logarithm of the isotopic separation factor is proportional to the length of the column. Thus,

$$\ln q = H_{ij} L/K \qquad (2)$$

where H_{ij} is the initial transport coefficient for separation of the nuclides i and j, and K is the remixing coefficient.

The data of Table II-4 were taken in two devices of identical construction except for length. Clearly, the relationship of Equation 2 does not hold for these experiments. For example, we would expect, on the basis of experiment S2, to get a separation

$$q = (1.236)^{114/15} = 5.00 \qquad (3)$$

for experiment L3; however, the observed separation, q = 1.647, is much lower than expected.

The most reasonable explanation for the discrepancy is that a portion of the experimental column has been rendered unstable as the result of parasitic convection caused by an unfavorable vertical density distribution. Such convection would take place at any location in the column where the solute concentration tended to increase in the upward direction, or when

$$dw_2/dz > 0 \qquad (4)$$

where z is the vertical coordinate, and w_2 is the solute concentration.

To examine this hypothesis in detail, it is necessary to do two things: 1) determine the behavior of the column coefficients as functions of concentration, and 2) develop a procedure for solving the differential equations which describe the steady-state behavior of the solute-solvent system.

In the previous report, we described a technique for obtaining the initial transport coefficient for the solute-solvent pair from measurements of the rate of change of the solute concentration at the bottom of the column during startup. A special set of short experiments was set up to obtain the data from the 114-cm column over a concentration range from 1.47 wt % $Ca(NO_3)_2$ to 43.5%. The resulting values of H_{ss}, the initial transport coefficient for the solute-solvent pair, are plotted in Figure II-2.

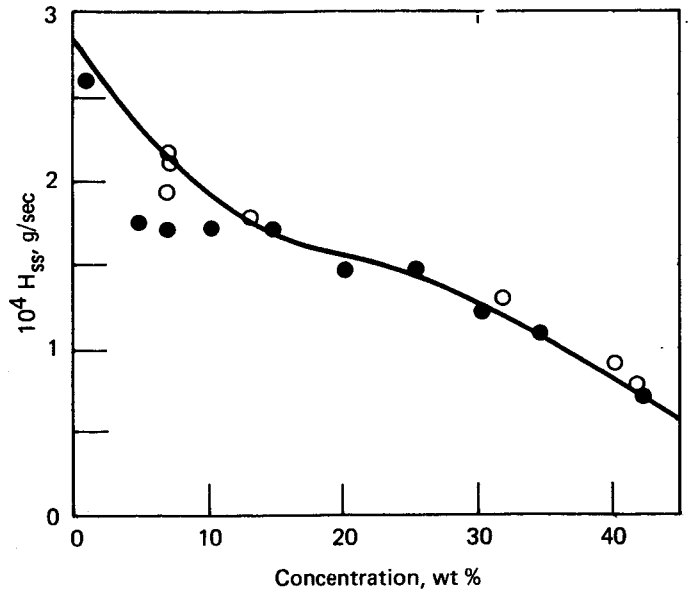

FIGURE II-2 - Initial transport coefficient for the aqueous $Ca(NO_3)_2$ system as a function of concentration.

Also plotted in Figure II-2 are values of H_{ss} derived from steady-state solvent counterflow experiments for which

$$H_{ss} = \frac{\sigma}{w_1} \tag{5}$$

where σ is the solvent injection rate, and w_1 is the mass fraction of solvent at the bottom of the column.

The two sets of data are not consistent over the whole concentration range. In drawing the curve in Figure II-2, preference was given to the solvent counterflow data.

The coefficient K was estimated based on a separation experiment done without counterflow in the 15-cm column. At an average concentration, w_2, of 14.9%, the equilibrium separation factor for $Ca(NO_3)_2$ - water was found to be given by

$$\ln q_{ss} = 7.077 \tag{6}$$

According to theory

$$\ln q_{ss} = \frac{H_{ss} L}{K} \tag{7}$$

Thus, K can be calculated for $w_2 = 14.9\%$.

To get K at other concentrations, we can use the following relationship based on the simple theory of the column.

$$K/K_o = [\rho (\frac{d\rho}{dT})^2/\eta]_{w_2} / [\rho (\frac{d\rho}{dT})^2/\eta]_{w_2}$$

$$= 14.9\% \tag{8}$$

The equation describing the counterflow separation process must be solved by numerical methods. The theory of the counterflow process requires that

$$\frac{dw_2}{dz} = \frac{-w_2[H_{ss}(1-w_2)-\sigma]}{K} \tag{9}$$

with $w_2 = (w_2)_T$ at $z = 0$.

A computer program was written and tested to solve Equation 9 by a 4th order Runge-Kutta method. The program includes procedures for table lookup and parabolic interpolation to get local values of H_{ss} and K as the integration proceeds.

The program was used to calculate the solute concentration gradient as a function of position in the column for each of four experiments of Table II-4. The results are plotted in Figure II-3 as functions of the relative position along the column.

We assume that the separation observed in an experiment results from a fraction of the length of the column and that the separation in the remainder of the column is destroyed by parasitic convection.

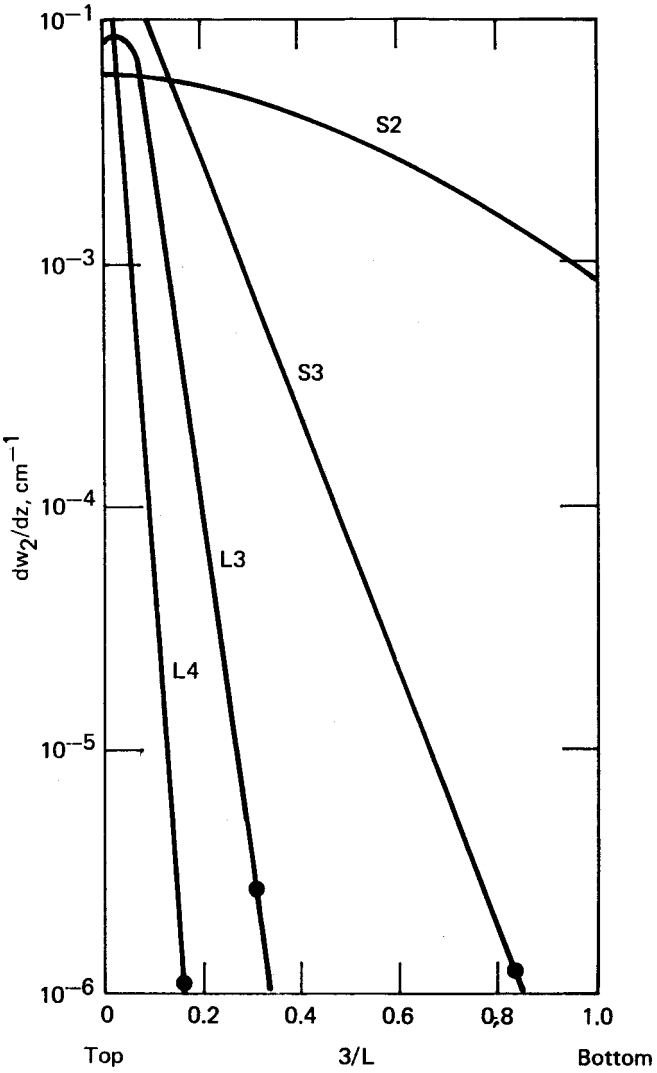

FIGURE II-3 - Calculated concentration gradients for calcium isotope separation experiments.

If we also assume that the separation of experiment S2 represents a fully functional column, then we can calculate an effective length for each of the remaining experiments. Thus,

$$(\ln q)_{FF} = \frac{L}{15} (\ln q)_{S2} \qquad (10)$$

where $(\ln q)_{FF}$ is the expected value for a fully functional column, and the effective length is given by

$$\frac{L_{EFF}}{L} = \frac{(\ln q)_{OBS}}{(\ln q)_{FF}} \qquad (11)$$

The ratio L_{EFF}/L is indicated for each experiment on Figure II-3 at the point of intersection with the gradient curve.

The obvious conclusion from Figure II-3 is that the column invariably becomes unstable when the density gradient becomes greater than that corresponding to a negative concentration gradient on the order of 3×10^{-4} wt %.

These results suggest that it will be difficult, if not impossible, to get stable operation of conventional thermal diffusion columns much longer than 15 cm. We believe, however, that stable operation can be obtained by manipulating the geometry of the column annulus. Experiments are now being set up to explore this alternative.

Zinc isotope separation

W. M. Rutherford

An exploratory experiment carried out last year [10] showed that dimethyl zinc is a potentially useful working fluid for the separation of zinc isotopes by liquid phase thermal diffusion. Dimethyl zinc is a volatile pyrophoric fluid; however, it seems to be reasonably stable in the typical operating temperature range of the liquid thermal diffusion column.

Work in progress is directed toward a further assessment of dimethyl zinc as a working fluid. The work has the following short range objectives: 1) to develop techniques for purifying, handling, and transferring the pyrophoric material; 2) to evaluate the stability of the fluid at the operating temperatures used in our prototype columns; and 3) to measure column parameters for use in predicting the performance of larger systems.

Experimental apparatus for evaluating the thermal diffusion behavior of dimethyl zinc was designed around an existing prototype column 70 cm in length with a hot-to-cold wall spacing of 254 μm. After the apparatus was installed, three separation experiments were completed using various techniques for purifying the fluid. The resulting isotopic separations were quite low and erratic. Subsequent measurements with a standard test fluid showed that the experimental column was not working properly. Another column has now been installed as a replacement, and additional experiments will be carried out in the near future.

Molecular beam scattering

R. W. York

TRIPLE-PUMPED DETECTOR

Installation of the support electronics was completed for the initial operation of the quadrupole detector during pumpdown. The detector housing was rough pumped to 10^{-6} torr by the main chamber vacuum system, then isolated by means of a manually operated gate valve that sealed the detector entrance from the main chamber. The three ion pumps on the detector housing were then used to independently evacuate the detector to its ultimate vacuum. The system was designed for an ultimate of 10^{-11} torr. During the final pumpdown, the main chamber was allowed to pressure up to 1 atm to test the vacuum integrity of the detector housing at 1 atm pressure differential. There was no rise in pressure in the housing, indicating that the detector was independently vacuum tight. This will allow future maintenance to be performed on the main chamber without disturbing the ultrahigh vacuum in the detector, saving lengthy pumpdown time.

The detector housing pressure leveled off at 5×10^{-9} torr and remained at that point for some time. The quadrupole, which had been operated during the pumpdown, showed a mass scan which appeared to contain fractions of high mass organics. The largest of these peaks was around mass 28. It was determined that residual contamination from the original fabrication [11] most probably produced excessive outgassing. Since the ultimate remained at 5×10^{-9} torr over a long period of pumping time, it became clear that the only effective way to remove this limiting outgassing contamination was to bake the detector housing at high temperature (350°C to 500°C) in a vacuum oven maintained at 10^{-5} torr or lower.

Before the assembly was removed from the main chamber, the multiplier ceased working. After removal, we found that the multiplier had been damaged by the large amounts of organic components that evolved during pumpdown. The multiplier has been sent to a vendor to be rebuilt, and arrangements are being made to remove the detector housing from the chamber and have it thoroughly vacuum baked.

Chemical exchange

G. C. Shockey and B. E. Jepson

MAGNESIUM CHEMICAL EXCHANGE WITH MACROCYCLIC LIGANDS

Magnesium chemical exchange with macrocyclic compounds was investigated. Three two-phase systems were examined (see Table II-5); and of these, the magnesium trifluoroacetate [$Mg(TFA)_2$], dicyclohexo 18-crown-6 (dch) in methylene chloride system showed the greatest potential for magnesium isotope enrichment. Distribution studies were done on this system, varying the magnesium and dch concentrations in order

Table II-5 - EQUILIBRIUM CONCENTRATIONS OF MAGNESIUM AND LIGANDS IN TWO-PHASE SYSTEMS

System	Phase	Mg M	Ligand, M	D(Mg)
1. $Mg(Cl)_2$/dch	Aqueous	3.83	0	0.008
	Organic	0.03	1.03	
2. $Mg(TFA)_2$/dch	Aqueous	3.07	0.09	0.05
	Organic	0.15	0.08	
3. $Mg(TFA)_2$/211	Aqueous	0.19	0.10	0.04
	Organic	0.007	0.007	

to find a stable system with a suitable distribution of magnesium into the organic phase (Table II-6). The exchange rate was found to be rapid with a half time of less than 0.5 min.

DISTRIBUTION STUDIES

An important criterion for the development of a two-phase chemical exchange process is that the desired element be distributed into both phases at high concentrations.

In general, magnesium does not complex well with macrocyclic polyether compounds; and the choice of these ligands is quite limited. An extensive listing of metal cation-macrocycle stability constants and other thermodynamic properties can be found in reference 12. The ligands investigated in this report are 211 cryptand and dicyclohexano 18-crown-6, hereafter referred to as 211 and dch, respectively. The structures of 211 and dch are shown in Figure II-4.

Table II-6 - CONCENTRATIONS OF MAGNESIUM IN THE $Mg(TFA)_2$/dch SYSTEM WITH HIGH dch CONCENTRATIONS

Phase	Mg, M	Ligand, M	D(Mg)
1) Aqueous	3.06	0.08	0.42
Organic	1.29	0.79	
2) Aqueous	3.06	0.11	0.25
Organic	0.78	0.50	
3) Aqueous	2.95	0.06	0.09
Organic	0.27	0.16	
4) Aqueous	2.26	—	0.03
Organic	0.08		
5) Aqueous	3.07	0.09	0.05
Organic	0.15	0.08	

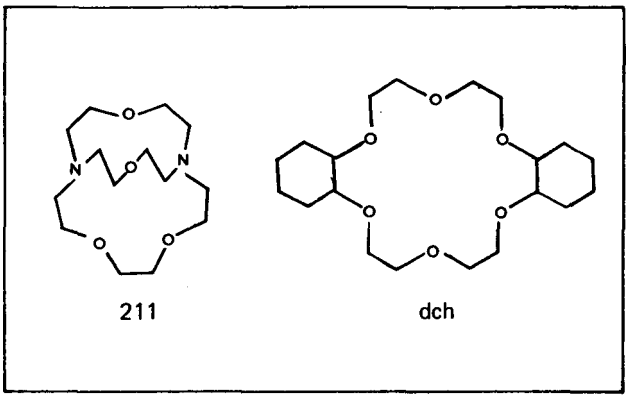

FIGURE II-4 - Structures of 211 cryptand and dicyclohexano 18-crown-6.

Although references in the literature do not indicate that magnesium complexes with dch [12], we have found that it does, in fact, complex under the experimental conditions used.

Three systems were examined: $Mg(Cl)_2$/dch, $Mg(TFA)_2$/dch, and $Mg(TFA)_2$/211. Each system examined (see Table II-5) was equilibrated by thoroughly mixing the two phases and allowing them to separate. Any phase volume changes were noted, and small samples were taken from each phase to determine the distribution of the magnesium and the ligand between the phases. Distribution coefficients (D) were calculated according to the following Equation 1:

$$D_{Mg} = \frac{[Mg^{++}]_{org}}{[Mg^{++}]_{aq}} \qquad (1)$$

The most promising of these systems was $Mg(TFA)_2$/dch, thus additional $Mg(TFA)_2$/dch systems were investigated in an attempt to obtain higher values of D. These results are shown in Table II-6. Of these, the system showing the most promise was 3.25 M aqueous $Mg(TFA)_2$ and 0.25 M dch in CH_2Cl_2 (#5 Table II-6).

The equilibrated two-phase system consisted of a 3.07 M $Mg(TFA)_2$ aqueous phase and a 0.15 M $Mg(TFA)_2$-complex organic phase. The species separation efficiency was 97%. The species separation efficiency is a measure of the degree to which each of the two species of the element to be separated (here, complexed and uncomplexed $Mg(TFA)_2$) is present in one of the two phases to the exclusion of the other. The presence of both species in a single phase reduces the separation factor of the process. The species separation efficiency (E) was determined using the expression:

$$E = (1 - N^{B}_{org} - N_{aq}^{A})\ 100\% \qquad (2)$$

where N^{B}_{org} is the fraction of $Mg(TFA)_2$ (uncomplexed) in the organic phase and N^{A}_{aq} is the fraction of $Mg(TFA)_2$ complexed with the ligand in the aqueous phase. In a blank equilibration with $Mg(TFA)_2$ and methylene chloride (no dch), the distribution of $Mg(TFA)_2$ into the organic phase was negligible. It was assumed, therefore, that all the magnesium in the organic phase was complexed.

In the $Mg(TFA)_2$/dch systems, increased dch concentrations resulted in improved distributions; however, seemingly stable supersaturated solutions can readily be formed, and such two-phase systems may remain in solution for hours, days, or months without signs of precipitates. Numbers 1 and 2 in Table II-6 were supersaturated with precipitation occurring after one or two days. The more dilute solutions formed only very small amounts of crystals over a two-to-four-month period. A longer term study of solution stability would be required to determine maximum concentrations attainable for unsaturated solutions.

It is interesting to note in Table II-6 that all the organic phase magnesium concentrations are greater than the dch concentrations. Since $Mg(TFA)_2$ is insoluble in methylene chloride, it is assumed that a two-to-one magnesium-to-dch complex is formed in the organic phase.

The use of the lipophilic TFA-anion appears to be important in complex formation. For example, $Mg(Cl)_2$, under similar conditions (#1 Table II-5) to those of the $Mg(TFA)_2$ systems, does not distribute to any practical extent into the organic phase. The magnesium concentrations in the organic phase are lower than desirable, leading to small distribution coefficients. Because of the low value of D, the $Mg(Cl)_2$/dch system was not studied further.

The third system investigated was $Mg(TFA)_2$/211 in methylene chloride. The macrocycle 211 was selected as a ligand for potential magnesium isotope enrichment both because of its favorable stability constant with magnesium ions [12] and its capacity of forming organic phase lithium complexes [13]. The $Mg(211)^{+2}$ complex, however, proved to be too soluble in the aqueous phase, leading to very low organic phase concentrations (Table II-5) and a species separation efficiency (Equation 2) of only 47%. Thus, the criterion that different species of the metal be distributed into each phase at high concentrations cannot be met. The solubility of 211 itself is enhanced by its two aza nitrogens, and the magnesium complex is doubly charged relative to the singly charged lithium complex, further increasing aqueous phase solubility.

HETEROGENEOUS EXHANGE RATE

A kinetics study was done with the $Mg(TFA)_2$/dch system. Initial concentrations of 3.08 M $Mg(TFA)_2$ and 0.25 M dch were used in this study. The procedure for evaluating the heterogeneous exchange rate kinetics has been previously described in more detail [13,14]. In general, the two phases were equilibrated by mixing them vigorously for 24 hr. Using enriched magnesium-25 as a tracer added to the organic phase, the phases were again mixed with samples drawn from both phases at different time intervals. The samples were converted to $Mg(NO_3)_2$, removing all the dch. Sodium contamination was removed, and the samples were analyzed for isotopic composition by mass spectrometry. The results are shown in Table II-7. Isotope exchange was shown to be complete within 0.5 min, which is sufficiently rapid for the purpose of this work.

Sodium contamination interferes with mass spectrometer measurements of magnesium isotope ratios and must be removed from the samples. A method for its removal has been established by the National Bureau of Standards (NBS) [15]. We found this to be an effective procedure. The procedure involved making a fairly concentrated (0.1 to 1 M) $Mg(NO_3)_2$ solution and adding ethylenediamine tetraacetic acid (EDTA) in the NH_4^+ form to precipitate the magnesium as magnesium dihydrogen ethylenediamine tetraacetate hexahydrate. The precipitate was then washed several times and filtered to remove any sodium. The sample was heated to 1000°C to remove the EDTA and to convert the sample to MgO. Finally, the samples were diluted to 5 mg/mL (as Mg) with 2N HNO_3 and

Table II-7 - EXCHANGE RATE KINETICS OF MAGNESIUM dch CHEMICAL EXCHANGE AT T = 25°C (Atom % Mg Isotope)

Time (min)	Mg 25		Mg 26	
	Org	Aq	Org	Aq
0	26.28	9.94	8.82	10.80
0.5	10.43	10.39	10.65	10.76
1.5	10.41	10.39	10.79	10.73
5.0	10.43	10.48	10.86	10.93
15	10.40	10.41	10.75	10.80
60	10.40	10.36	10.77	10.77
180	10.43	10.38	10.87	10.73
480	10.38	10.38	10.73	10.69
1440	10.39	10.37	10.73	10.70

analyzed by mass spectrometry. We found that the precipitation would not occur if either the $Mg(NO_3)_2$ or the EDTA was too dilute, the pH of the EDTA too high, or if the pH of the $Mg(NO_3)_2$-EDTA mixture was not within the pH range of 3.5 to 5.5. We used 0.1 to 1 M $Mg(NO_3)_2$ and 0.5 M EDTA with a pH of 6.0. The NBS procedure [15] states that approximately 5% of the magnesium is left in solution, but that mass spectrometric examination shows that the isotopic composition of the magnesium in solution is identical with that of the precipitated magnesium so that no significant fractionation occurs during the sample preparation.

A single-stage separation has been completed for the $Mg(TFA)_2$/dch system. Sample analysis for isotope ratio by mass spectrometry is in progress to determine the single-stage separation factor (α).

Liquid extraction column development for calcium isotope enrichment

R. J. Tomasoski and E. D. Michaels

Calcium isotope enrichment by chemical exchange techniques based on Jepson's work appears only to await the development of suitable hardware for phase contacting and phase reflux. Performance criteria for extraction columns to be used in calcium isotope enrichment are as follows:

(1) Column throughput must match the flow requirement of the cascade – in practical terms, this means small columns with capacities of 5-20 mL/min.

(2) Stage residence time must be low enough to permit cascade equilibrium in a reasonable time – in practical terms, this means residence times of 10 sec or less.

Both requirements are outside the normal range of parameters for conventional liquid extraction columns. A literature survey indicated the best chance of success lay in the application of rotary annular extraction columns to the problem.

To ensure that both performance criteria have been met, it is necessary to measure the hydraulic capacity of flooding, (V_c+V_d), the mass transfer coefficient (Ka), and the axial dispersion coefficient, E_c. The throughput requirement is determined directly from (V_c+V_d):

$$Q = \pi(r_o^2-r_i^2)(V_c+V_d) \tag{1}$$

and the residence time is determined as

$$T_r = \frac{\frac{V_c}{(Ka)} + \frac{E_c}{V_c}}{(V_c+V_d)} \tag{2}$$

To determine these parameters, a mathematical model was developed to allow simultaneous determination of mass transfer and axial dispersion coefficients, and an experimental column was fabricated and is currently undergoing testing.

MATHEMATICAL MODEL

To pursue the investigation of mass transfer phenomena and axial dispersion phenomena in countercurrent liquid-liquid columns, it is necessary to have a usable mathematical description of the transport processes involved. The similarity between countercurrent liquid-liquid operations and fixed bed liquid-solid operations suggests that the theory previously developed for fixed bed processes might be used. The major drawback to this approach is that it restricts the disperse phase to plug flow and ascribes all observed axial dispersion phenomena to the continuous phase. This approach has been employed in the past, as disperse phase phenomena tend to be smaller than continuous phase phenomena.

The derivation of the model starts by considering a volume containing the two phases with a disperse phase volume ratio $(1-\varepsilon)$. Conservation of mass requires

$$\frac{D}{Dt}\int_v \left[\varepsilon c + (1-\varepsilon)c_d\right]dv = 0 \tag{3}$$

where D/Dt is the substantial derivative operator. Applying the transport theorem for a region containing a singularity [16] moving at velocity u_ξ yields

$$\int_v \frac{\partial}{\partial t}(\varepsilon c)dv + \int_s (\varepsilon c)\vec{V}_c ds - \int_{SING} [\varepsilon c]u_\xi ds$$

$$+\int_v \frac{\partial}{\partial t}(1-\varepsilon)c_d dv + \int_s (1-\varepsilon)c_d\vec{V}_{cd}ds$$

$$-\int_{SING} [(1-\varepsilon)c_d]u_\xi ds = 0 \tag{4}$$

If we specify that the coordinate system is stationary with respect to the disperse phase, then the velocity of the singular surface is $u_\xi = 0$, and the velocity of the disperse phase is also $v_d = 0$; hence,

$$\int_v \left[\varepsilon\frac{\partial c}{\partial t} + \varepsilon\nabla\cdot\vec{V}_c c + (1-\varepsilon)\frac{\partial c}{\partial t}d\right]dv = 0 \tag{5}$$

Since V is arbitrary, the integrand must equal zero

$$\varepsilon\left(\frac{\partial c}{\partial t}\right) + \varepsilon\nabla\cdot\vec{V}_c c + (1-\varepsilon)\frac{\partial c}{\partial t}d = 0 \qquad (6)$$

Invoking Fick's law yields

$$\varepsilon\left(\frac{\partial c}{\partial t}\right) + \varepsilon\nabla\cdot c\vec{V} + (1-\varepsilon)\frac{\partial c}{\partial t}d = \varepsilon D\nabla^2 c \qquad (7)$$

Neglecting gradients in the θ and r directions and requiring incompressible flow results in simplified form

$$\varepsilon D\left(\frac{\partial^2 c}{\partial z^2}\right) = \varepsilon V\left(\frac{\partial c}{\partial z}\right) + \varepsilon\left(\frac{\partial c}{\partial t}\right) + (1-\varepsilon)\left(\frac{\partial c}{\partial t}d\right) \qquad (8)$$

This is the equation used as a starting place for the analyses of Lapidus and Amundson [17] and Van Deemter et al. [18]

Lapidus and Amundson found the following solution to the above equation (with boundary conditions corresponding to a pulse input)

$$\left(\frac{C}{C_o}\right) = \frac{zt_o}{2t\sqrt{\pi Dt}}\, e^{-\frac{z(-vt)^2}{4Dt} - \frac{Kat}{\varepsilon}} + \int_o^t \frac{zt_o}{2t'\sqrt{\pi Dt'}} e^{-\frac{(z-vt')^2}{4Dt'}} F(t')dt' \qquad (9)$$

where

$$F(t') = \sqrt{\frac{(Ka)^2 K_D t'}{\varepsilon(1-\varepsilon)(t-t')}}\, \exp\left\{-\frac{(Ka)K_D(t-t')}{(1-\varepsilon)} - \frac{(Ka)t'}{\varepsilon}\right\} I_1\left\{2\sqrt{\frac{(Ka)^2 K_D t'(t-t')}{\varepsilon(1-\varepsilon)}}\right\}$$

Van Deemter et al. have shown that, for values of z much larger than (2D/v) and (εv/Ka), Lapidus and Amundson's solution reduces to

$$\left(\frac{C}{C_o}\right) = \frac{\beta t_o}{\sqrt{2\pi(\sigma_1^2+\sigma_2^2)}}\, e^{-\frac{(z/v-\beta t)^2}{2(\sigma_1^2+\sigma_2^2)}} \qquad (10)$$

where

$$\frac{1}{\beta} = 1 + \frac{(1-\varepsilon)}{\varepsilon K_D}$$

$$\sigma_1^2 = 2\frac{Dz}{v^3}$$

$$\sigma_2^2 = 2\beta^2\frac{(1-\varepsilon)^2 z}{\varepsilon Kav K_D^2}$$

To adapt this result to a liquid-liquid process with the disperse phase moving with respect to the laboratory with velocity v_D, the transformations

$$z \rightarrow x+v_d t \text{ and } v = v_c+v_d \qquad (11)$$

are introduced. The simplified form of the response to a tracer pulse thus becomes

$$\left(\frac{C}{C_o}\right) = \frac{\beta t_o}{\sqrt{2\pi(\sigma_1^2+\sigma_2^2)}} \exp\left[-\frac{1}{2}\frac{\left(\frac{x+V_d t}{V_c+V_d} - \beta t\right)^2}{(\sigma_1^2+\sigma_2^2)}\right] \qquad (12)$$

where

$$\frac{1}{\beta} = 1 + \frac{(1-\epsilon)}{\epsilon K_D}$$

$$\sigma_1^2 = 2\,\frac{D(x+V_d t)}{(V_c+V_d)^3}$$

$$\sigma_2^2 = 2\beta^2 \frac{(1-\epsilon)^2 (x+V_d t)}{\epsilon Ka\,(V_c+V_d) K_D^2}$$

This equation has the form of the Gaussian error function with mean, $(x-\mu)$, of

$$\left(\frac{x+V_d t}{V_c+V_d} - \beta t\right) \qquad (13)$$

and variance σ^2 of

$$(\sigma_1^2 + \sigma_2^2) \qquad (14)$$

For the special case of chemical exhange of calcium isotopes $v_c=v_d$ and $\epsilon/(1-\epsilon)=2$ so that these equations simplify to:

$$\left(\frac{C}{C_o}\right) = \frac{\beta t_o}{2\pi\sqrt{(\sigma_1^2+\sigma_2^2)}}\, e^{-\frac{\left(\frac{x}{2v} - (\beta-\frac{1}{2})t\right)^2}{2(\sigma_1^2+\sigma_2^2)}} \qquad (15)$$

where

$$\beta = \frac{2K_D}{2K_D+1}$$

$$\sigma_1^2 = \frac{D(x+vt)}{4v^3}$$

$$\sigma_2^2 = \left(\frac{\beta^2}{6}\right) \frac{x+vt}{(Ka)\,k_D^2 v}$$

The axial dispersion coefficient D (contained in the function σ_1^2) and the mass transfer coefficient Ka (contained in the function σ_2^2) may be simultaneously determined by measurements of the response to a tracer input at two axial positions, x_1 and x_2.

EXPERIMENTAL

This study had two purposes: to determine the feasibility of using a rotary annular column as a contactor in a calcium enrichment cascade and to determine the optimum parameters for its use.

The rotary annular column (RAC) was selected because it theoretically combines a low holdup volume with a high extraction efficiency. The column consists of a rotating shaft inside a stationary coaxial outer tube. The shear forces created by the rotating shaft set up a pattern of stable vortexes in the annular gap. These shear forces also break the dispersed phase into small droplets and disperse them into the vortex pattern.

The column along with its testing system is shown in Figure II-5. The column has an effective length of 2 ft. The stainless steel rotor is 8 mm in diameter, and the annular gap between the rotor and the glass outer tube is 2 mm. The column has disengaging zones at either end to separate the phases. These consist of a housing with an expanded annular gap of 11 mm and a rotor sleeve to reduce turbulence. The rotor is driven by a variable speed electric motor. The phase interface is located in the top housing just above the organic inlet and is controlled by adjusting the organic flowrate into the column. The column is fed from pressurized feed bottles. A constant volume pump was installed at the organic outlet to ensure a constant flowrate of the continuous phase through the column.

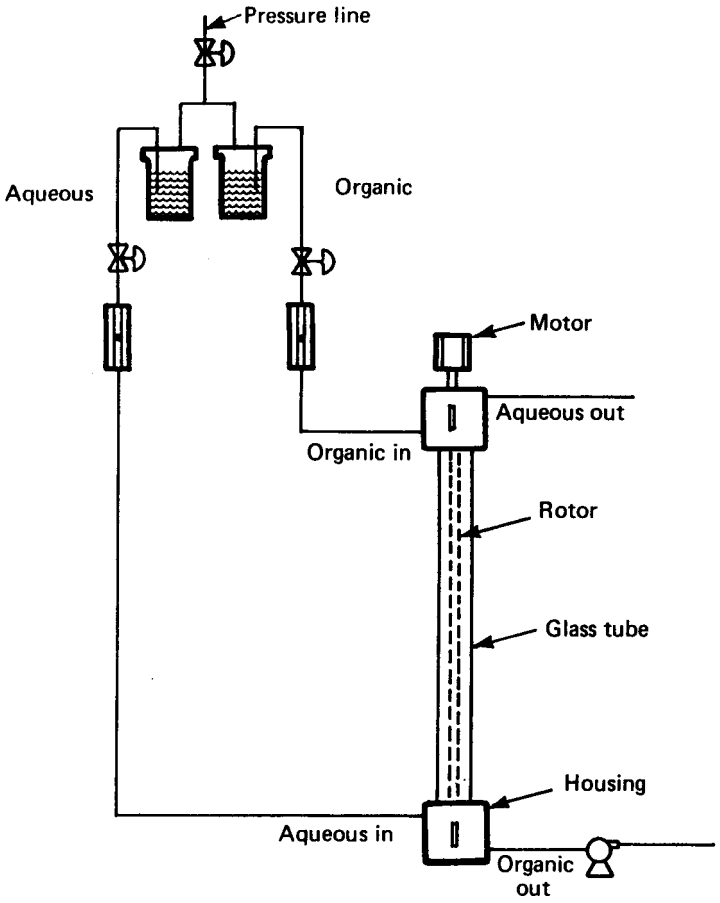

FIGURE II-5 - Column and testing systems.

After the column and test system procedures had been established and stable column operation achieved, experiments were performed to establish a flooding curve for the column. Flooding was determined visually by observing the point at which the aqueous stream no longer flowed upward into the column but rather was forced into the bottom housing by the organic stream. The points on the curve shown in Figure II-6 were found by allowing the column to achieve steady-state conditions for a particular set of flowrates, then slowly increasing the rotor speed until flooding occurred. The values produced in this manner have proved to be reproducible.

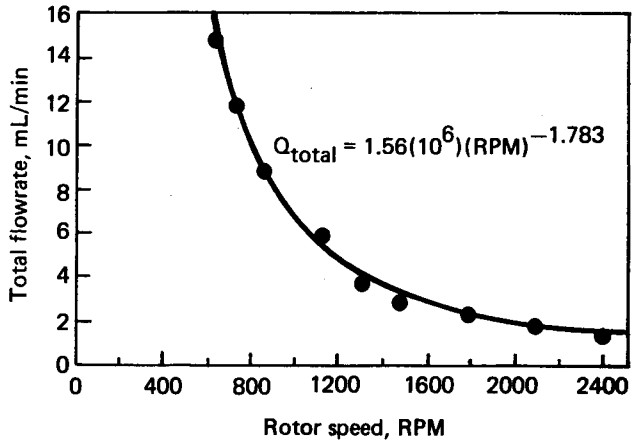

FIGURE II-6 - Flooding curve for 2-mm gap column.

NOMENCLATURE

C	solute concentration in continuous phase
C_d	solute concentration in disperse phase
$\vec{V}_c$	continuous phase solute velocity
V_d	dispense phase velocity
$\vec{V}$	continuous phase mass velocity
ε	continuous phase volume fraction
(Ka)	interphase mass transfer coefficient
D	axial dispersion coefficient
β	mass transfer parameter
σ_1, σ_2	dispersion parameters
v_d	average disperse phase velocity

Reflux of NO-HNO_3 chemical exchange system

E. D. Michaels and R. H. Nimitz

INTRODUCTION

Present processes for producing enriched nitrogen-15 suffer poor scale-up economics. The NO distillation process used in the

United States operates at cryogenic temperatures and, as currently operated, uses the irreversible evaporation of liquid nitrogen to effect the top reflux. The NO-HNO_3 chemical exchange process, which is widely used in Europe, uses an open reflux which requires the use of SO_2 as a reagent and produces dilute H_2SO_4 as a by-product.

The basic scale-up problems for both of these processes are associated with the reflux. A new reflux process based on electrochemical reduction in solid polymer electrolyte (SPE) cells has been proposed by Mound personnel for the reflux of the NO-HNO_3 chemical exchange process. The purpose of this work is to demonstrate the applicability of this concept to the reflux of chemical exchange systems by:

(1) Presenting a feasible process flowsheet;
(2) Demonstrating experimentally that the electrochemical reduction process works;
(3) Measuring the performance parameters of the electrochemical reduction process; and
(4) Estimating the economics of a pilot-scale (100 kg/yr nitrogen-15) plant and small commercial-scale plants based on this technology.

PROCESS DESCRIPTION

The closed cycle reflux of the NO-HNO_3 chemical exchange system requires the production of nitric oxide, NO, from nitric acid, HNO_3, without the concomitant production of by-product chemicals. By using solid polymer electrolyte cells (shown schematically in Figure II-7), it is possible to reduce HNO_3 to its reagent components (NO_2, H_2O, and O_2) in the following set of electrochemical reactions:

Anode half reaction:

$$H_2O \rightarrow 2H^+ + 2e + 1/2\ O_2$$

Cathode half reaction:

$$HNO_3 + 3H^+ + 3e \rightarrow NO_{(g)} + 2H_2O.$$

By using the SPE electrolytic reactor in conjunction with a drying column to separate NO and H_2O, as shown schematically in Figure II-8, it is possible to produce NO for the separation cascade with the co-production of the stoichiometric amounts of oxygen and water required to produce HNO_3 from NO at the top of the isotope separation cascade. The reflux is thus closed at both ends of the isotope separation cascade and requires no additional reagents and produces no waste streams.

Initial tests of the SPE electrolytic reactor with pure HNO_3 revealed that its overvoltage was too high to be of use in an economic process. Subsequently, all work was performed with multivalent metal ions as a catalyst for the reduction reaction. The modified chemical reactions are as follows:

Anode half reaction:

$$H_2O \rightarrow 2H^+ + 2e + 1/2\ O_2$$

Cathode reactions (with copper ions):

$$3Cu^{2+} + 3e \rightarrow 3Cu^+$$
$$3Cu^+ + HNO_3 + 3H^+ \rightarrow 3Cu^{2+} + NO_{(g)} + 2H_2O$$

No attempt was made to determine the mechanisms of the reactions involved. The above reactions are representative of the overall reaction and not intended to describe the specific mechanism, which undoubtedly involves other nitrogen

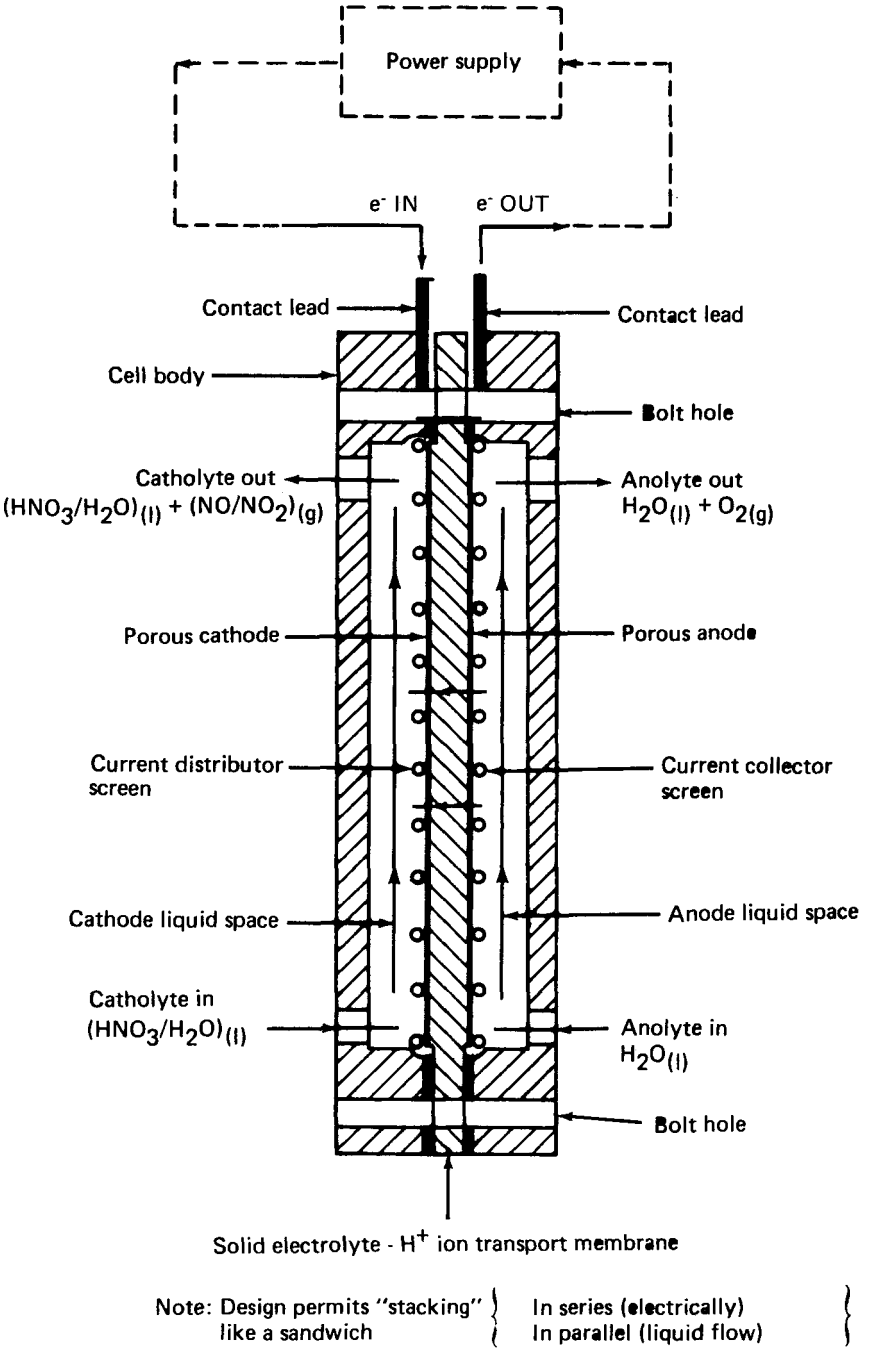

FIGURE II-7 - Schematic of electrolytic reactor.

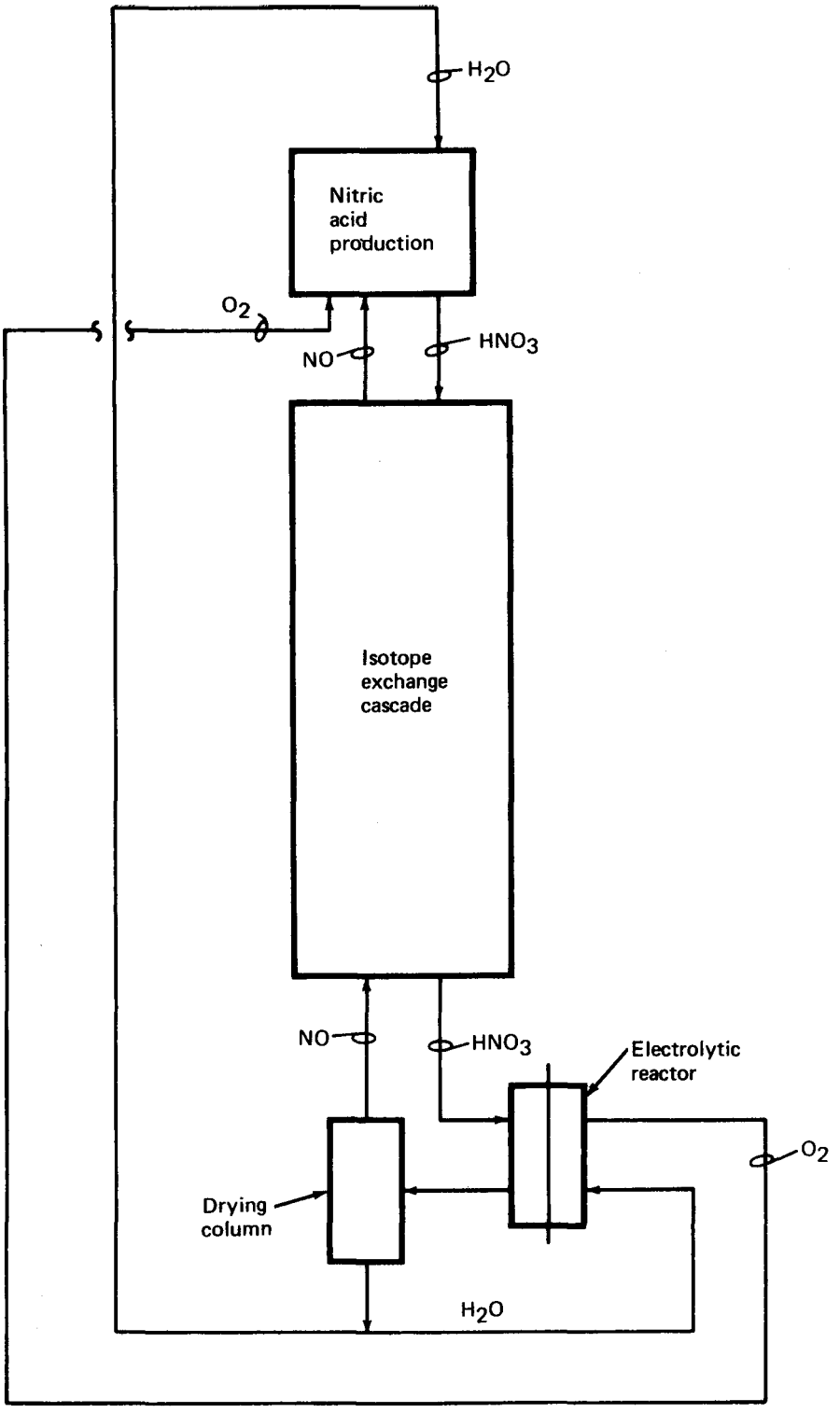

FIGURE II-8 - Closed loop reflux schematic.

oxidation states. The modifications required of the process flowsheet are shown in Figure II-9.

EXPERIMENTAL SYSTEM

To determine the conditions under which the SPE electrolytic reactor could be operated to produce reflux for the $NO-HNO_3$ chemical exchange process, a batch reactor loop was used. The lay-out of this experiment is shown in Figure II-10. Primary components of the test loop were: the electrolytic reactor with cation exchange membrane separator, HNO_3-NO and H_2O-O_2 phase separators, a constant current power supply, a gas receiver to collect the nitrogen oxides produced, and a wet-test meter to measure the amount of oxygen evolved from the cathode.

The electrolytic reactor, shown in Figure II-10, had an active surface area of 45.6 cm^2 per cell so that the change in acid composition was very slow compared to the residence time of the cell. Since the cell behaves as a differential reactor, rate data could be collected on the basis of compositions measured external to the reactor without loss of accuracy. The standard procedure was to set the current density at a fixed value, and then record pressure and temperature in the gas receiver, oxygen flow from the anode compartment, cell voltage and temperature, and HNO_3 composition as a function of time. At the conclusion of each run, gas samples were collected from the gas receiver for analysis by infrared absorption spectra.

The major parameters which control the economics of electrolytic reflux for the Nitrox chemical exchange process are the current efficiency, which is defined as

$$\theta_i = \frac{\text{equivalents of } NO_x \text{ vapor produced*}}{\text{faradays expended}}$$

and the voltage efficiency, which is defined as

$$\theta_v = \frac{\text{equilibrium voltage}}{\text{terminal voltage}}$$

*The equilibrium NO_x vapor composition in equilibrium with 10M nitric acid is a mixture of NO, NO_2, N_2O_4, and N_2O_3. This equilibrium has been calculated by Stern [19].

Current efficiency was determined by measuring the rate of production of NO_x (dP/dt in the gas receiver) and the composition of the NO_x (by infrared analysis of grab samples) as a function of the faradays of charge passed through the reactor. Typical pressure as a function of faraday (or time at constant current) plots are shown in Figure II-11. At no time was hydrogen observed in the grab samples. The low NO_x production rate during the initial part of the experiment resulted from the reaction of NO with the liquid HNO_3 to establish the equilibrium liquid phase composition [19].

Data collected at 400, 600, and 800 A/ft^2 with copper nitrate as a catalyst indicate current efficiencies of 100% in all cases. Table II-8 gives average experimental values for a number of runs and conversions. Terminal voltage was measured as a function of current density for three different cell configurations. Data for copper catalyzed runs for all three cells are shown in Figure II-12.

The first cell used was a standard water electrolysis cell manufactured by the aircraft equipment division of General

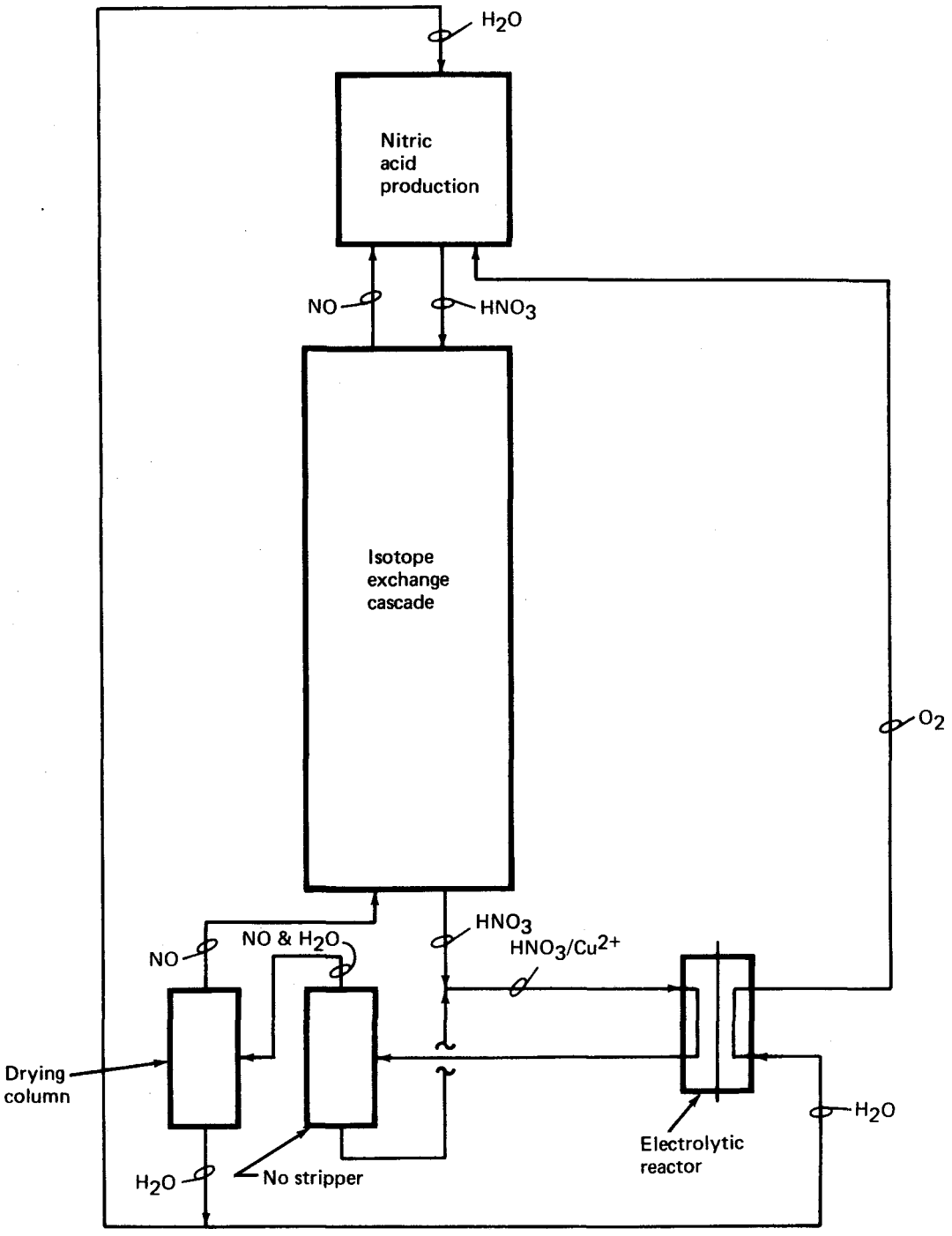

FIGURE II-9 - Closed loop reflux schematic with Cu catalysis.

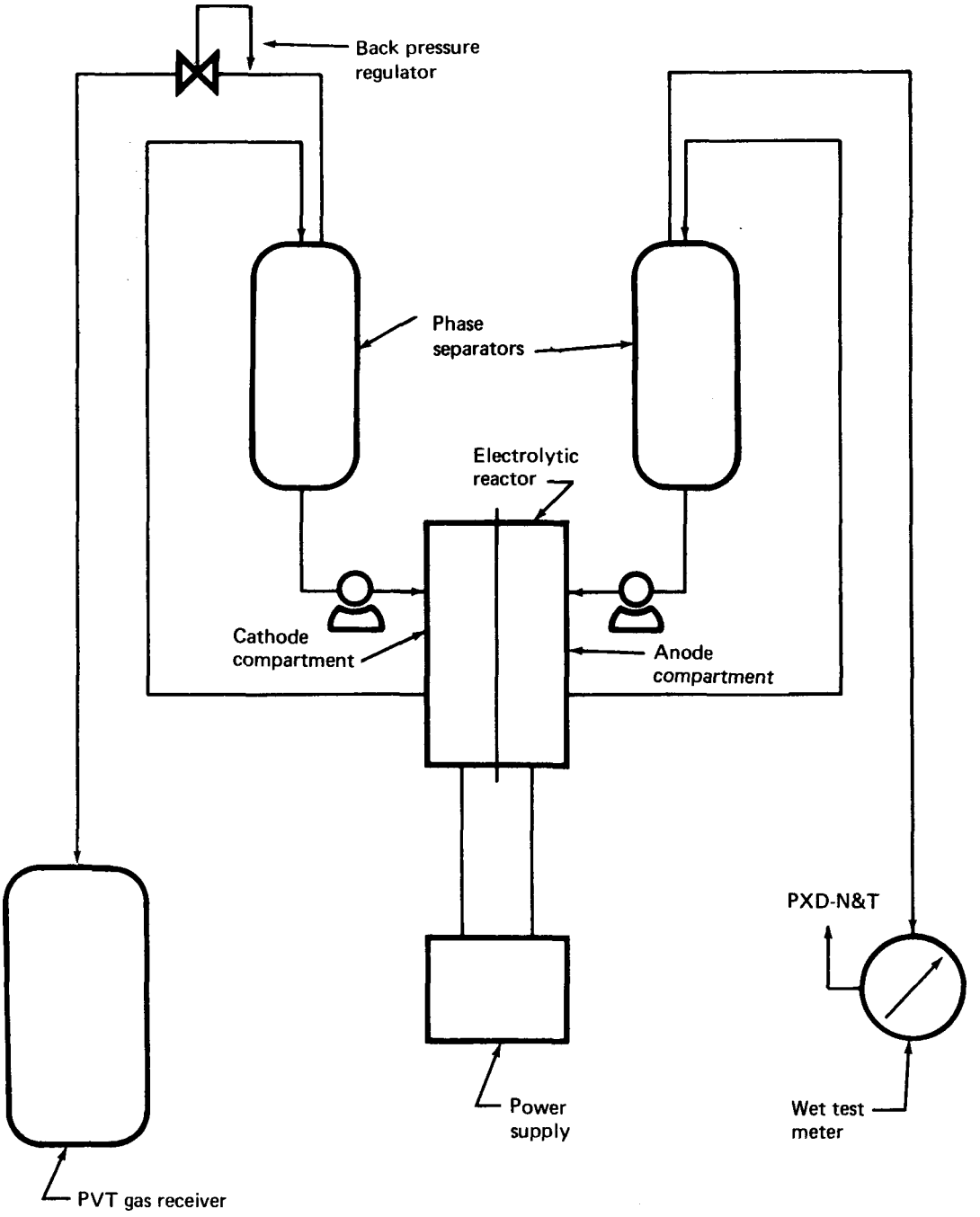

FIGURE II-10 - Flow schematic of test system.

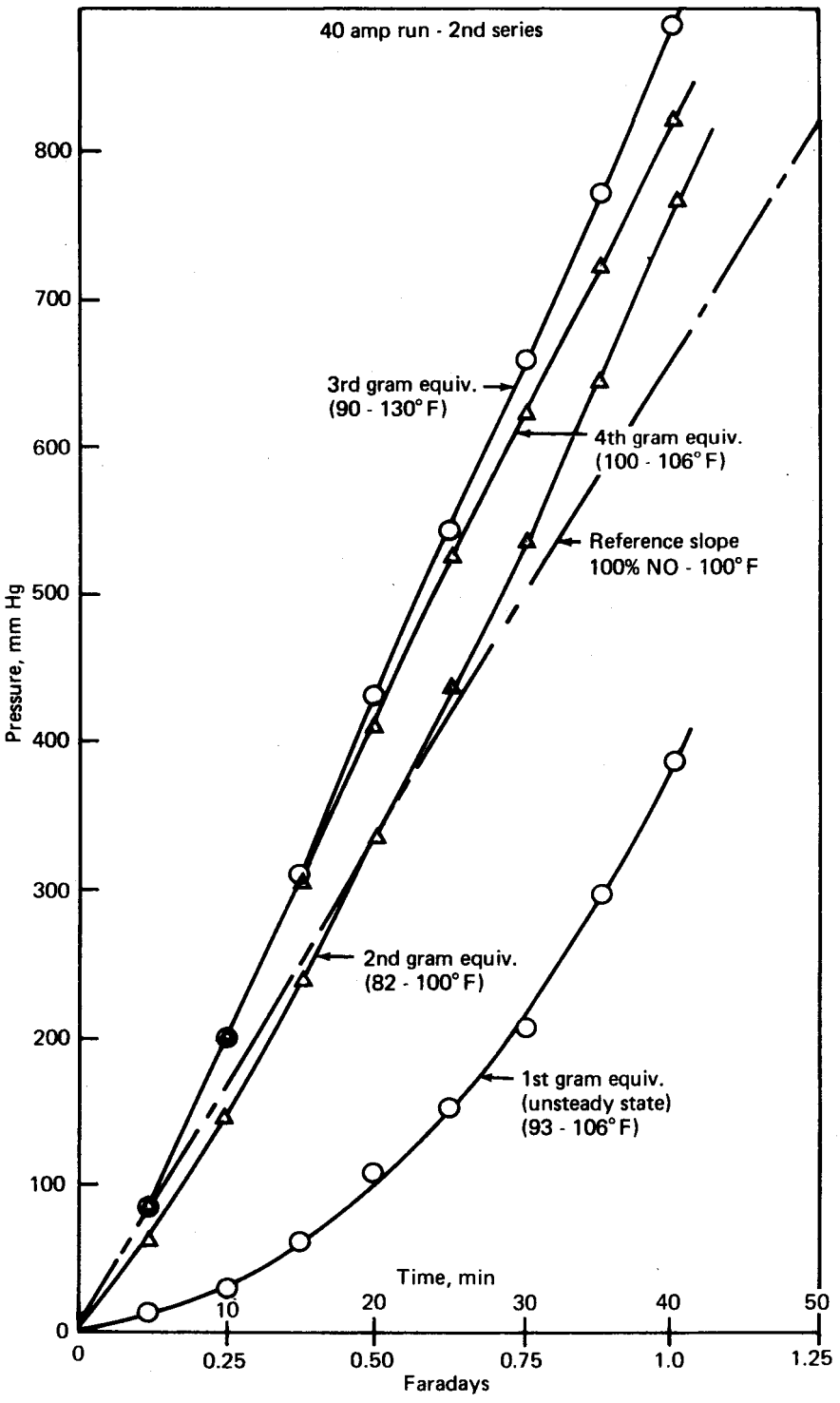

FIGURE II-11 - Current efficiency was determined by measuring the rate of NO_x production.

Table II-8 - EXPERIMENTAL CURRENT EFFICIENCIES FOR VARIOUS CURRENT DENSITIES

Current Density (A/ft^2)	1st Gram Equivalent	2nd Gram Equivalent	3rd Gram Equivalent
400	97%	101%	100%
600	100%	93%	96%
800	102%	96%	103%

Electric Company. This cell is constructed with tantalum current collectors and other wetted parts, which were passivated by the nitric acid solutions, resulting in high cell resistance.

The second cell, also supplied by General Electric, was constructed of a Kynar/graphite composite material with the current collectors machined as an integral part of the cell body (small pyramids on a 1-cm square pitch). The voltage drop across this cell improved substantially (see Figure II-12).

To assess the impact of mass transfer on the observed voltage drop, a third test cell was fabricated. This cell, which was also formed from the Kynar/graphite composite, had parallel flow channels molded into the cell body with current collector ridges separating each flow channel. Tests with this hardware indicate the lowest voltage drops observed to date (see Figure II-12).

OPTIMUM OPERATING POINT

To proceed with an analysis of the economic impact of the present technology, it will be necessary to establish the optimum current density. The optimum operating point is a balance between operating cost, which increases with current density, and capital cost, which

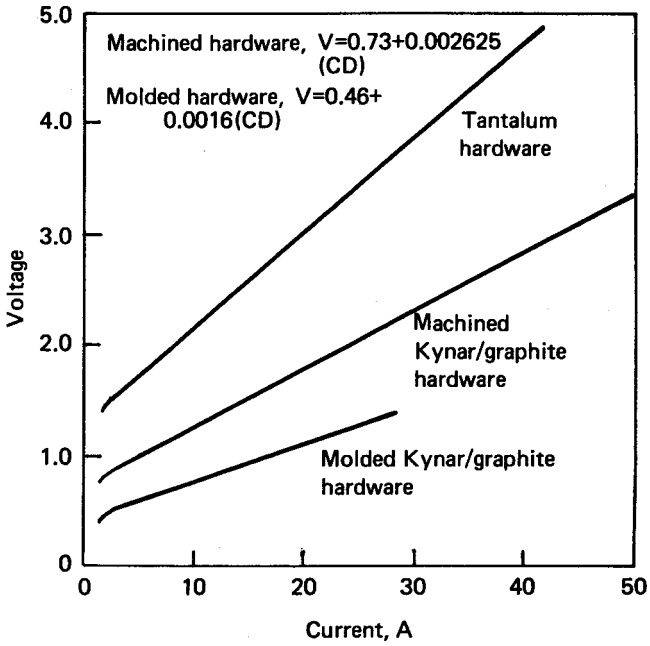

FIGURE II-12 - Terminal voltage drop for copper catalyzed runs.

decreases with current density. Assuming \$0.045/kW-hr electricity, the total cost of the reflux operation for a plant producing 20 kW of nitrogen-15 per yr is expressed as

$$TC = 20{,}805 + 72.5(CD) + \frac{18{,}680}{(CD)} (RC)$$

where

CD = current density, A/ft^2

TC = total annual cost, \$

RC = unit reactor cost, $\$/ft^2$

General Electric is developing similar electrolytic reactors with SPE membranes for electric utility peaking service and has estimated unit costs for prototype reactors to vary from approximately $\$2400/ft^2$ for a pilot-scale module to less than $\$200/ft^2$ for large commercial units manufactured on a production basis. The optimum current density as a function of electrolytic reactor unit cost, shown in Figure II-13, can be found by setting $\partial(TC)/\partial(CD) = 0$ and solving for CD to yield

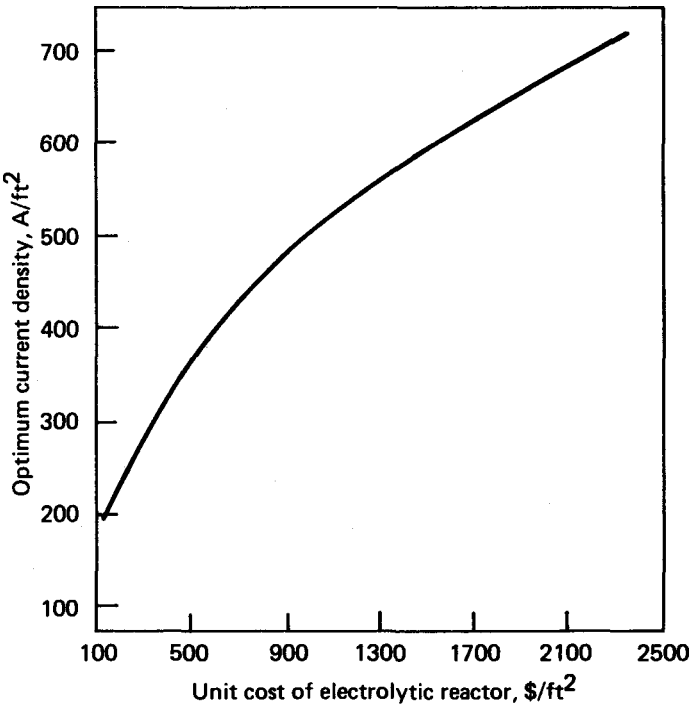

FIGURE II-13 - Variation in optimum current density with capital cost of electrolytic reactor.

$$CD_{op} = 253(RC)$$

The most probable cost per square foot is on the order of $\$250/ft^2$ for an electrolytic reactor of the size required for a plant producing 20 kg of nitrogen-15 per yr. The optimum operating point would thus be approximately 250 A/ft^2.

ECONOMICS OF 20 KG/YR PLANT

Based on isotope separation theory, a conceptual plant design was completed to assess the economic merit of the Nitrox process with electrolytic reflux. The plant design was based on the flowsheet shown in Figure II-14. The separation cascade in this plant is provided by two columns. The first is 13.3 cm in diameter and 21 m high; the second is 3.8 cm in diameter and 24 m high. The intermediate and product refluxes are provided by electrolytic reduction, and the tails reflux is provided for by a small nitric acid plant.

The cost of all major capital equipment items is detailed in Table II-9. Through the use of Lang factors, the fixed capital cost of the plant was estimated to be \$1,130,000. The manufacturing cost of nitrogen-15 produced in such a plant would be the sum of the amortization rate and the operating costs (manpower, feed, utilities, maintenance, etc.). Assuming a straight line amortization for 10 yr with a 10% time value of money results in an annual capital recovery rate of 16.275% per yr. The operating costs, summarized in Table II-10, are estimated at \$300,000 per yr. The net fund cost for nitrogen-15 produced in such a plant would thus be \$24.20/g. This is a substantially lower cost than that associated with the nitrogen-15 produced by cryogenic distillation.

Removal of plutonium from solution by adsorption on boron phosphate

G. L. Silver

Bone char and many other calcium phosphate compounds effectively remove 99% or more of the plutonium in aqueous solution [20]. The purpose of this work is to examine boron phosphate, BPO_4, as an adsorbent for plutonium. Boron phosphate possesses a potentially useful advantage over other phosphate adsorbents, namely, it is slowly decomposed by water

$$BPO_4 + 3HOH = H_3BO_3 + H_3PO_4 \qquad (1)$$

so that, in principle, the adsorbent can be easily separated from the adsorbed radioactive pollutant by dissolution of the adsorbent after decontamination operations have been completed. Were an operation such as decontamination by adsorption, followed by adsorbent dissolution possible, a substantial reduction in volume of solid radioactive waste

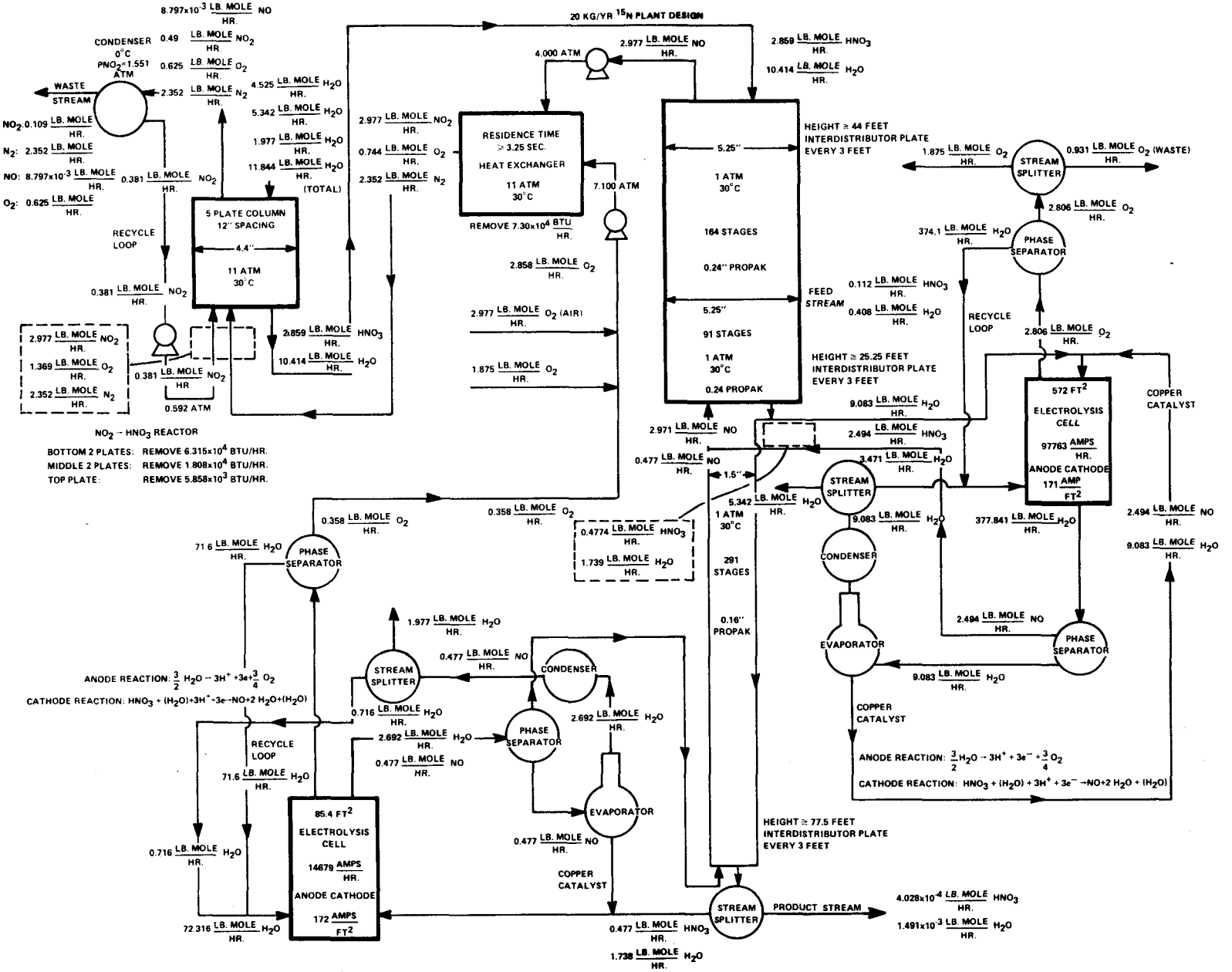

FIGURE II-14 - Plant design flow sheet.

Table II-9 - MAJOR CAPITAL EQUIPMENT AND COST FOR A 20 KG/YR NITROGEN-15 PLANT

Column, SS, 3.8 cmϕ	$ 13,000
Column, SS, 13.3 cmϕ	12,000
Packing for columns, Propak	7,200
Distributor plates	5,300
Electrolysis cells, 460 SF	114,000
NO_2 scrub column	2,000
Evaporators	35,000
Phase separators and splitters	6,000
Diaphragm compressors	40,000
Condenser	4,000
Subtotal	$238,500

Table II-10 - NITROX PLANT OPERATING COST

Utilities	$100,000
Manpower	50,000
Analytical laboratory	20,000
Feed cost	20,000
Maintenance	25,000
Overhead	85,000
	$300,000

could be realized. Moreover, the adsorbent could be regenerated by the reverse of Equation 1. Unfortunately, it appears that boron phosphate is not well suited for this purpose because of incomplete removal of the pollutant, as well as slow kinetics of adsorption.

Boron phosphate samples were purchased from the Sharpe Chemicals Company, Burbank, CA. The material was received as lumps of a white solid. A sample of this material was ground in a mortar, and the particles were sieved to obtain particles of more or less the same size. The particles selected for study passed through a sieve having holes of 850 μm, but were retained by a sieve with holes of 500 μm. A gram of the material was weighed into a 100 mL flask, and deionized water added. During the next several days, the flask was shaken frequently. After three days of exposure to water, only a cloudy solution with a few particles of undissolved BPO_4 remained in the flask. After one week, the BPO_4 was completely dissolved, and the liquid in the flask was clear. The

solution had a low pH, as would be expected if dissolution had occurred by the hydrolysis represented by Equation 1.

The rate of dissolution of BPO_4 appears to be accelerated by alkali. BPO_4 placed in water, and in dilute alkali, and then gently heated indicated that, in warm water, the dissolution reaction was accelerated by bases such as potassium hydroxide. Boron phosphate can be made resistant to dissolution if it is ignited, and most descriptions of BPO_4 record this fact [21-25]. Samples of BPO_4 were therefore ignited at 300°C for 1 hr (Sample "A"), at 600°C for 1 hr (Sample "B"), and at 1100°C for 1/2 hr (Sample "C"). Heating BPO_4 causes it to lose weight. For example, a sample of BPO_4 heated to 1000°C for 1 hr lost 13% of its original weight. Material heated to 1000°C for 1 hr does not noticeably dissolve in boiling water, even after 20 min of boiling. The addition of a few pellets of KOH to the water did not appear to have any effect on the rate of dissolution during a second boiling period of 20 min.

Boron phosphate easily forms emulsions. These stable suspensions give liquids in contact with BPO_4 a milky appearance. This phenomenon is troublesome, because liquid sampled from containers containing BPO_4 is frequently turbid, and the effluent from columns of BPO_4 is similarly milky. If, however, an ammonium nitrate solution is passed through a column of BPO_4, the effluent gradually becomes clear. The presence of the electrolyte prevents peptization of the BPO_4 as a colloid, and the more concentrated the NH_4NO_3 solution, the clearer the effluent from the column. Material ignited at 1000°C also showed this effect, although it did not peptize as badly as the "as received" material.

A sample of "as received" BPO_4 was ground and sieved as described above. It was then washed in a beaker with 1M NH_4NO_3 solution until the washings were clear. This material was then transferred to a small column. When 0.1M NH_4NO_3 solution was passed through the column, the effluent was "very turbid." When 0.2M NH_4NO_3 was passed through the column, the effluent was "turbid." When 0.3M NH_4NO_3 was passed through the column, the effluent was "somewhat turbid," and when 1M NH_4NO_3 was passed through the column, the effluent was "faintly turbid." Although only qualitative, these observations suggest that the presence of electrolytes is essential in solutions to be decontaminated by BPO_4. Unfortunately, polyvalent electrolytes can compete with dissolved radioactive materials rendering the adsorption operation much less effective. Finally, when pure water was passed through the column, the effluent was so turbid that it looked like milk.

A sample of "as received" BPO_4 was ground and sieved as described above. It was washed in the sieve with tap water until the washings had lost most of the initial turbidity. (This was accomplished with substantial loss of BPO_4.) The remaining solid was then dried at 110°C for 1 hr. Samples of this dried material weighing 0.6 g were transferred to 100 mL flasks. Into one flask was placed distilled water. This produced immediate clouding. Into another flask was placed 0.125M NaCl solution. This produced slow clouding. Into a third flask was placed 0.25M NaCl solution. This produced slower clouding. Into yet another flask was placed 0.5M NaCl solution. This did not produce clouding to any extent considered significant. After two days, most of the BPO_4 in all the flasks had dissolved, but the relative cloudiness of each solution did

not seem to be affected by the dissolution reaction.

This qualitative experiment was repeated using BPO_4 (ground and sieved) which had been ignited at 300°C for 1 hr. The results were similar, although complete dissolution of the material was not observed. Also, the appearance of cloudiness in the solution took much longer. Table II-11 summarizes the results and shows that electrolytes can be used to control peptization of the BPO_4. Even the dissolved minerals in tap water exert a noticeable effect. Table II-11 also shows that ignition of the BPO_4 renders it less reactive to water, as the establishment of the final degree of cloudiness was not complete after one day, although it appeared to be instantaneous with "as received" material. The ignition of inorganic materials frequently renders them less reactive, or more "inert." This is an advantage in controlling cloudiness, but a disadvantage in adsorption processes, as "inert" materials can be poor adsorbents because their surface reactivity has been destroyed by the annealing effect of high temperature.

One-gram portions of Sample "A" described above were placed in 100 mL flasks in the presence of a trace of plutonium-239 dissolved in a sodium acetate, ethylene diammine buffer. It was intended to study the adsorption of the plutonium as a function of pH. After one day of frequent and vigorous shaking, the samples were allowed to stand overnight (to allow the cloudiness to settle in the hope of sampling a clear solution). Samples of the solutions were withdrawn and analyzed for residual plutonium content. The pH of the first flask of the series was measured and found to be 5.42. After shaking for a second day, and again allowing to stand overnight, each solution was sampled for residual plutonium-239 content and pH. The results of this experiment are shown in Table II-12. It is to be observed that the first solution, which had a pH of 5.42 after one day, had a pH of 3.84 after the

Table II-11 - REACTION OF BPO_4 IN FOUR SOLVENTS
BPO_4 IGNITED AT 300°C FOR ONE HOUR.

Flask contents, 0.6-g BPO_4 plus	Observation after One day	Observation after One week
Distilled HOH only	some cloudiness	opaque
Distilled HOH, 0.125M NaCl	little cloudiness	very cloudy
Distilled HOH, 0.25M NaCl	clear	cloudy
Distilled HOH, 0.5M NaCl	clear	slightly cloudy
Tap HOH only	little cloudiness	cloudy
Tap HOH + 0.125M NaCl	clear	somewhat cloudy
Tap HOH + 0.25M NaCl	clear	slightly cloudy
Tap HOH + 0.50M NaCl	clear	slightly cloudy

Table II-12 - PLUTONIUM REMOVED FROM SOLUTIONS CONTACTED WITH BPO_4 (SAMPLE "A"). SOLUTIONS CONTAIN 0.25M NaCl[a]

Solution No.	Percent (%) Plutonium absorbed after One day	Two days	pH
1	57	57	3.84
2	44	54	3.60
3	45	54	3.63
4	51	60	3.25
5	45	56	3.32
6	43	57	2.84
7	39	60	2.69
8	47	64	2.73
9	43	66	2.46
10	48	76	2.22
11	60	81	2.02

[a]The initial plutonium-239 count was 33,000 d/min/500 .

second day. Evidently the BPO_4 was slowly dissolving according to Equation 1. The degree of plutonium adsorption is disappointing, amounting to only about one-half of the plutonium initially present in the flasks. The kinetics of adsorption also appear to be slow. But prolonged contact times are not permissible because they render column operations impractical.

A second absorption experiment was attempted using BPO_4 Sample "B" (ignited at 600°C for 1 hr). The solutions contained 0.20M NaCl and 0.1M ethylene diammine buffer. As can be seen from Table II-13, the extent of plutonium removal by BPO_4 is disappointing. These experiments were repeated with BPO_4 Sample "C" in both acidic and alkaline media. Tables II-14 and II-15 indicate the results.

To test the extent of plutonium adsorption by BPO_4 over longer periods, nine flasks were prepared as follows: three each contained 1 g of BPO_4 Sample "A", three each contained 1 g of BPO_4 Sample "B", and three each contained 1 g of BPO_4 Sample "C." Three buffers were also prepared. Buffer "A" had a pH of 5.5, Buffer "B" a pH of 8.0, and Buffer "C" a pH of 10.0. Samples of the buffers were added to the flasks as indicated in Table II-16. Plutonium-239 was also added to each flask such that the initial plutonium count in each flask was 13,200 d/min/500λ. These flasks were then allowed to stand for one week with frequent shaking. At the end of the week, each flask was sampled for residual plutonium concentration in the liquid phase, and the pH of each solution was also measured. As can be seen from Table II-16, the final

Table II-13 - PLUTONIUM REMOVED FROM SOLUTIONS CONTACTED WITH BPO_4 (SAMPLE "B") AFTER A TWO DAY EQUILIBRATION PERIOD (0.20M NaCl)

Solution No.	Activity removed (%)	pH
1	35	9.95
2	38	9.85
3	49	9.55
4	59	9.08
5	52	8.51
6	53	8.22
7	53	8.04
8	58	7.78
9	57	7.35
10	62	6.91

[a]The initial plutonium-239 count was 33,000 d/min/500 .

Table II-14 - PLUTONIUM REMOVED FROM SOLUTIONS CONTACTED WITH BPO_4 SAMPLE "C" (NO SALT ADDED)[a]

Solution No.	Percent (%) Plutonium adsorbed after One day	Two days	pH
1	19	36	10.55
2	15	33	10.40
3	15	30	10.06
4	28	41	9.55
5	38	50	8.57
6	44	59	7.95
7	40	57	7.75
8	38	52	7.46
9	46	63	7.15
10	39	57	6.63

[a]The initial plutonium-239 count was 33,000 d/min/500 .

Table II-15 - PLUTONIUM REMOVED FROM SOLUTIONS CONTACTED WITH BPO_4 SAMPLE "C" (NO SALT ADDED)[a]

Solution No.	Percent (%) Plutonium adsorbed after Two days	One week	pH
1	44	71	5.70
2	30	51	5.66
3	36	59	5.65
4	37	57	5.59
5	47	63	5.45
6	55	75	5.20
7	50	71	4.70
8	61	80	2.85
9	55	74	2.15
10	57	73	2.11
11	61	74	2.09
12	60	70	1.90

[a]The initial plutonium-239 count was 33,000 d/min/500 .

Table II-16 - REMOVAL OF PLUTONIUM-239 FROM SOLUTIONS EXPOSED TO SAMPLES OF BPO_4 FOR ONE WEEK

Flask No.	BPO_4 Sample	Buffer	% Plutonium removed	Final pH
1	A	A	93	2.65
2	A	B	93	3.45
3	A	C	93	4.70
4	B	A	80	3.45
5	B	B	79	4.42
6	B	C	80	5.25
7	C	A	72	4.90
8	C	B	70	5.60
9	C	C	93	8.00

pH of each solution was lower than the initial pH, reflecting in part the BPO_4 dissolution reaction. This effect was greatest for BPO_4 ignited at 300°C, and least for the BPO_4 ignited at 1100°C.

Most of the plutonium had been adsorbed by the BPO_4 samples during the course of the week, but the extent of plutonium removal does not compare to plutonium removal by bone char.

III. Metal hydride studies

Prediction of nonmagnetic kondo effect in metal hydrides

G. C. Abell

In previous work [1], we proposed that the behavior of hydrogen in the Vb metals (V, Nb, Ta) could be understood in terms of a model, whereby a localized Jahn-Teller (JT) resonance state associated with metal atom d-orbitals is stablized by interstitial hydrogen. A simple model study [2] supported the plausibility of this idea, but there is as yet no direct experimental support. In view of this latter fact and of the novelty of the basic concept, it must be considered highly speculative for now.

On the basis of the similarity [2] of the JT Hamiltonian to the Anderson Hamiltonian (H_A) for magnetic impurities in metals [3], one might expect a Kondo effect -- identifiable by a logarithmic increase of resistivity with decreasing temperature -- for the former.

The purpose of this report is to show in simple terms, yet with some degree of mathematical rigor, that the Jahn-Teller (JT) polaron impurity can indeed give rise to a Kondo-like resistivity effect. We will be using an approach that was first applied to show the relation of H_A to the Kondo Hamiltonian (H_K). This approach takes the conduction band states of the lattice, together with the isolated impurity, as the zeroth order problem and treats the mixing term (i.e., the term that represents the hopping of an electron from the band states to the impurity and vice-versa) as the perturbation. The perturbation expansion is generated by a certain unitary transformation, known as the Schrieffer-Wolff (SW) transformation [4]. Before applying this approach to the JT polaron Hamiltonian, (H_{JT}), we study its application to H_A.

$$H_A = \sum_{ks} \varepsilon_k n_{ks} + \sum_{s} \varepsilon_d n_{ds} + U n_{d\uparrow} n_{d\downarrow} + \sum_{ks} (V_{kd} C^{\dagger}_{ks} C_{ds} + V^{*}_{kd} C^{\dagger}_{ds} C_{ks}), \quad (1)$$

where ε_k and ε_d are the one-electron energies of the conduction and localized orbitals, respectively, measured relative to the Fermi energy (ε_F). The d and k states are mixed by the potential V (V_{kd} is the hopping energy); U is the Coulomb repulsion between opposite-spin electrons on the d-orbital. The operators $C^{\dagger}_{ks}C_{ks}$) and $C^{\dagger}_{ds}(C_{ds})$ create (destroy) electrons in the states $|ks\rangle$ and $|ds\rangle$ respectively; $n_\alpha = C^{\dagger}_{\alpha} C_{\alpha}$ is the number operator for the state $|\alpha\rangle$. We also write

$$H_A = H_{cond} + H_{ion} + H_{mix} = H_o + H_{mix}.$$

The term H_{ion} (the 2nd and 3rd terms of Equation 1) represents the full Hamiltonian for an isolated impurity ion in any charge (i.e., q = o or q = ±e), and H_{mix} is a one-body operator which allows electrons to hop on and off the impurity atom, changing its charge by ±e. Schematically, the problem is as shown in Figure III-1 with distinct manifolds of states for the neutron ion ($S_z \equiv n_{d\downarrow} - n_{d\uparrow} = \pm 1/2$) and for the charged ion ($S_z = 0$; $n_d = 0,2$). The potential V couples the different manifolds. Table III-1 shows a submatrix involving antiparallel spin orientations; Table III-2 shows one with parallel spins. First, note that there are no direct matrix elements connecting states belonging to the ground state manifolds ($S_z = \pm 1/2$). Second, notice that the energy of the system will be lower for antiparallel spins because there are more matrix

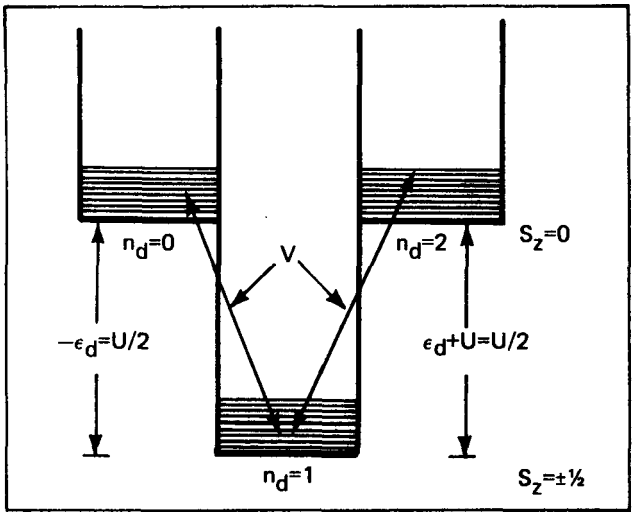

FIGURE III-1 - Manifold of states of the symmetric Anderson model when the impurity level width is zero. The thick lines represent states in which the conduction band is in its ground state, but the impurity orbital configuration corresponds to occupancy n_d = 0, 1, or 2. The orbital energy ϵ_d represents the difference of the many-body ground states n_d = 1 and 0. For each impurity configuration, the conduction band can also be a continuum of many-body excited states, indicated by the light lines lying at higher energy. The three sets of states overlap in energy. The inclusion of V causes transitions between the states as indicated by the diagonal arrows. (From H. R. Krishnamurthy et al., Phys. Rev. B, 21, 1044 (1980).

elements connecting ground manifold states to states of the S_z = 0 manifold, compared to the case of parallel spins. We thus have antiferromagnetic coupling of the impurity to the metal.

The SW transformation [4], in effect, folds the off-diagonal matrix elements of Table III-1 into the ground manifold, giving terms $\propto V^2/U$ connecting states within one of the S_z = ±1/2 manifolds and also connecting states of S_z = 1/2 to those of S_z = -1/2. These latter terms are spin-flip matrix elements; it is these that give rise to the Kondo effect. The collection of matrix elements thus obtained for the ground manifold may more conveniently be represented by an effective Hamiltonian, operating only on states belong to the S_z = ±1/2 manifolds. This Hamiltonian is through 1st order in V/U:

$$H_{eff} = \sum_{ks} \epsilon_k n_{ks} + \sum_{s} \epsilon_d n_{ds} - \sum_{kk'} J_{kk'}$$

$$\times \{(c^{\dagger}_{k'\uparrow} c_{k\uparrow} - c^{\dagger}_{k'\downarrow} c_{k\downarrow}) S_z$$

$$+ c^{\dagger}_{k'\uparrow} c_{k\downarrow} S_- + c^{\dagger}_{k'\downarrow} c_{k\uparrow} S_+ \}, \quad (2)$$

Table III-1 - SUBMATRIX OF H_A FOR ANTIPARALLEL SPINS

$k\uparrow,d\downarrow$ |	$\epsilon_k+\epsilon_d$	0	V	V*
$k'\downarrow,d\uparrow$ |	0	$\epsilon_{k'}+\epsilon_d$	-V	-V*
$d\uparrow,d\downarrow$ |	V*	-V*	$2\epsilon_d$+U	0
$k\uparrow,k'\downarrow$ |	V	-V	0	$\epsilon_k+\epsilon_{k'}$

Table III-2 - SUBMATRIX OF H_A FOR PARALLEL SPINS

$k\uparrow,d\uparrow$ |	$\epsilon_k+\epsilon_d$	0	V*
$k'\uparrow,d\uparrow$ |	0	$\epsilon_{k'}+\epsilon_d$	-V*
$k\uparrow,k'\uparrow$ |	V	-V	$\epsilon_k+\epsilon_{k'}$

where

$$J_{kk'} = V_{k'd}V^*_{kd}\left\{(\varepsilon_k-\varepsilon_+)^{-1} + (\varepsilon_{k'}-\varepsilon_+)^{-1} - (\varepsilon_k-\varepsilon_-)^{-1} - (\varepsilon_{k'}-\varepsilon_-)^{-1}\right\} \quad (3)$$

and

$$\varepsilon_+ = \varepsilon_d + U,\ \varepsilon_- = \varepsilon_d.$$

(In the symmetric Anderson model limit, $\varepsilon_d = -U/2$; Figure III-1 refers to this limit.) S means the spin operator of the impurity atoms, and $S_\pm$ the usual spin raising and lowering operators.

$$S_\pm = S_x \pm iS_y.$$

Actually, there are other terms $\propto V^2/U$ given by the SW transformation, which are not explicitly shown in H_{eff} because their effect is merely to shift the ε_k and ε_d. H_{eff} may appear somewhat formidable, but if $J_{kk'}$ is replaced by a constant J (a reasonable approximation which does not change the essential aspects of the problem), H_{eff} has the form of the Kondo Hamiltonian. The usual perturbation expansion [5] to 2nd order (in J) of H_K then reveals the logarithmic divergence at a characteristic temperature $kT_K \sim D\cdot\exp(-1/|N(0)\cdot J|)$, where 2D is the bandwidth. This expression assumes a constant density of states N(0) for the conduction band; a nonessential limitation. It also assumes that spin-flip scattering, as given by $J_{kk'}$ is possible for all $|\varepsilon_k-\varepsilon_{k'}|\leq D$. This latter assumption explains the presence of the cutoff factor D in the definition of T_K. Actually, the appropriate cutoff for the Anderson Hamiltonian is somewhat different from this [6]. Later on, we argue that for the JT Hamiltonian, spin-flip scattering is limited to a very restricted range of processes, and that the appropriate cutoff is $|\varepsilon_k-\varepsilon_{k'}|\leq h\omega_D$ (the Debye frequency). In concluding this section, we note that while the SW mapping of H_A onto H_K apparently requires [4] $|N(0)J|<<1$, it has been demonstrated [6] that this mapping is relevant far beyond the range of its derivation and applies even when $|N(0)J|\simeq 1$.

We now apply the SW method to the JT polaron Hamiltonian, (H_{JT}), given by [7]

$$H_{JT} = H_{cond} + H_{ion} + H_{mix} \quad (4)$$

where now

$$H_{ion} = \sum_s \varepsilon_d n_{ds} + \lambda(n_{d+}-n_{d-})(b^\dagger+b) + \omega_o b^\dagger b. \quad (5)$$

H_{cond} and H_{mix} are the same as before, except that the index s now refers to the two rows of the degenerate $\Gamma(E)$ representation of the D_{2d} point group to which the JT impurity belongs. (Orbitals belonging to $\Gamma(E)$ occur in pairs, corresponding to spatial degeneracy of the point group.) The index corresponding to electron spin is suppressed, as there are no spin dependent interactions in H_{JT}. The phonon creation operator b^+ corresponds to a localized Einstein oscillator with frequency ω_o. The parameter λ is the strength of the linear JT coupling interaction which is itself proportional to the difference in occupancies of the two JT orbitals and to the symmetry-lowering displacement coordinate Q_{JT} ($Q_{JT} \propto b^\dagger+b$). Because electron spin is suppressed, the number operators n_{ds} take the values, 0, 1, or 2. The relevant JT interaction energy analogous to the Coulomb energy

U of H_A is the quantity $C \equiv 2\lambda^2/\omega_o$. For the sake of discussion, consider the case with $C >> |V_{kd}|$. Then the uncoupled conduction band plus impurity provides a useful zeroth-order representation. How do we characterize the isolated ion in this case? Figure III-2 is a configurational representation of the isolated 'molecule' showing the adiabatic energy surfaces for the various molecular states as a function of the JT displacement coordinate Q_{JT}. The curves are labeled by the corresponding total occupancy $n_{JT} \equiv n_{d+} + n_{d-}$ and psuedospin $S_z \equiv (n_{d+} - n_{d-})/2$. The $n_{JT} = 1,3$ curve implies a Coulomb repulsion for these charge states. In fact, Coulombic effects should be largely screened out. Beneath the various minima are shown the molecular structures corresponding to the appropriate extremum values of Q_{JT}.

The lowest few oscillator levels in each well are also depicted. The solid and dashed lines represent two quite distinct kinds of transitions that are possible for this molecular system. The solid line corresponds to a Franck-Condon process for which the excitation freqency is much larger than ω_o; the transition takes place in such a short interval that structural relaxation is not possible. Thus, it is a vertical process and, as such, cannot provide an intermediate state for the pseudo spin-flip process $S_z = +1 \rightarrow S_z = -1$. The dashed lines, on the other hand, correspond to adiabatic processes for which the excitation frequency is much smaller than ω_o; the structure relaxes adiabatically to the relevent minimum. These processes do provide intermediate states for $S_z = +1 \rightarrow S_z = -1$, and thus are of special interest in the present study.

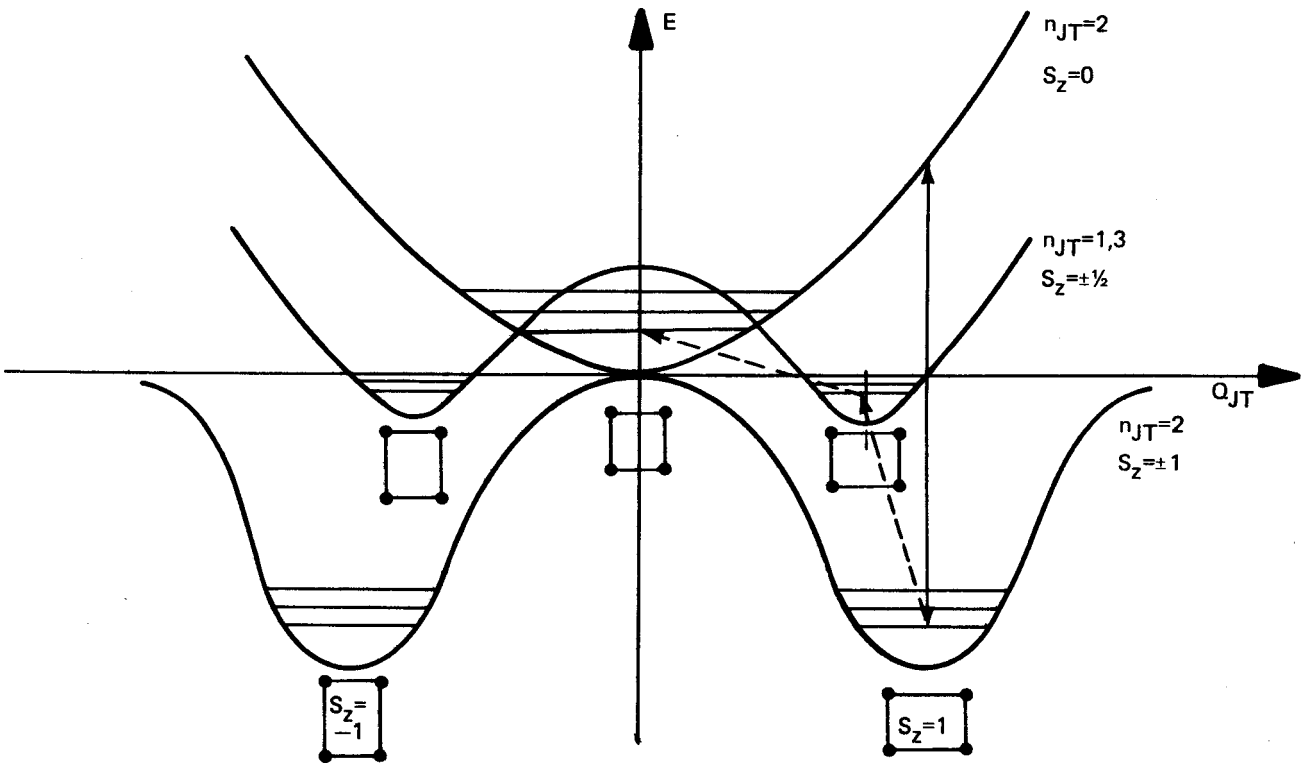

FIGURE III-2 - Electron and phonon states of the isolated JT impurity.

The mixing term in H_{JT} couples the distinct manifolds corresponding to $S_z = 0, \pm 1/2, \pm 1$; but now, in doing perturbation theory, we must carefully distinguish between virtual excited states corresponding on the one hand to vertical processes and on the other to adiabatic processes. We do that in the following way: virtual excitations for which the energy change of the scattered particle, $|\varepsilon_k - \varepsilon_{k'}|$, is less than ω_o correspond to adiabatic processes. Otherwise, they are vertical (Franck-Condon) processes. The same sort of distinction is made [8] in treating the electron-phonon interaction in the BCS theory of super-conductivity, so this is not a new idea.

Figure III-2 implies that two distinct adiabatic steps are required for the spin-flip: one for $S_z = 1 \rightarrow S_z = 0$, and the other for $S_z = 0 \rightarrow S_z = -1$. If this is true, then the effective operator corresponding to the pseudo spin-flip process is a two-body term rather than the one-body term (in $C^{\dagger}_{k'}C_k$) of the Kondo Hamiltonian. Such a term would not be expected to contribute to the resistivity. But the foregoing discussion supposes that the terms in the perturbation expansion corresponding to vertical processes are unimportant.

The SW transformation of H_{JT} is [4]

$$\tilde{H}_{JT} = e^{T} H_{JT} e^{-T}$$

such that in the basis which diagonalizes H_o (unspecified for now),

$$\langle \beta | T | \alpha \rangle = \langle \beta | H_{mix} | \alpha \rangle / (E_\alpha - E_\beta). \qquad (6)$$

H_{mix} is such that $|\alpha\rangle$ and $|\beta\rangle$ belong to different manifolds with $|E_\alpha - E_\beta| \approx C$.

Thus, to 2nd order, the matrix element connecting two distinct states belonging to manifolds having the same value of S_z^2 is

$$\langle b | H_{JT} | \alpha \rangle = E_a \delta_{ab} + 1/2 \sum_c \langle b | H_{mix} | C \rangle \langle C | H_{mix} | \alpha \rangle$$

$$\times [(E_a - E_c)^{-1} + (E_b - E_c)^{-1}] + \ldots \qquad (7)$$

Let us now define H_o such that this expansion includes only those terms for which $|\varepsilon_k - \varepsilon_{k'}| < \omega_o$ (i.e., terms corresponding to vertical processes are excluded). Representing all such terms symbolically by the operator h, we now write

$$H_o = H_{JT} - h. \qquad (8)$$

Now recognizing that $|\varepsilon_k - \varepsilon_{k'}|$ ranges from 0 to D (2D is the bandwidth), it is clear that h represents only a small fraction ($\approx \hbar\omega_o / D$) of all possible terms. Thus, we solve H_o simply by applying the usual adiabatic approximation (i.e., that the electrons adjust instantaneously to the structure) to H_{JT}, as if <u>all</u> the virtual excitations correspond to vertical processes. Consider an interval during which there are no slow processes occurring. In that case, our prescription for determining H_o gives the slow JT Hamiltonian studied in a previous paper [7]. One finds a stable polaron resonance with configurational degeneracy corresponding to $\langle S \rangle = \pm p (0 \leq p < 1)$, where the quantity p must be determined self-consistently. This result thus defines the ground state manifolds for our zeroth order Hamiltonian $H_o = H_{JT} - h$.

Now, consider an interval defined by a process for which $|\varepsilon_k - \varepsilon_{k'}| < \hbar\omega_o$ and for which the initial state belongs to $S = +p$. The virtual excitation thus

corresponds to an electron in the impurity orbital $|d->$ (or to a hole in $|d+>$). The impurity adjusts adiabatically to this slow occupation, and the electrons of the surrounding medium adjust adiabatically to the new impurity configuration. In other words, the relevant impurity potential for slow processes is determined not merely by the adiabatic adjustment of Q_{JT} as shown in Figure III-2, but also by the adiabatic response of the electrons as given by vertical processes. To obtain the extremum impurity configuration corresponding to the slow occupation, we write

$$2S \equiv \langle n_{d+} - n_{d-} \rangle = \int^{\varepsilon_F} d\varepsilon [2\rho_{d+}(\varepsilon;S) - \rho_{d-}(\varepsilon;S)] - 1, \quad (9)$$

In Equation 9, ρ_{ds} is the projection of the total density of states onto $|ds>$, as described in reference 7. So long as $S > 0$, we can definitely assign the "slow electron" to the orbital $|d->$. But for $S = 0$, this is no longer possible; the two orbitals $|d+>$ and $|d->$ share the excitation so that $S = 0$ is always a self-consistent solution. There may be another solution in the range $0 < S \leq 1/2$; in the limit $C >> |V_{kd}|$, the effective impurity potential will be essentially as shown in Figure III-2. But in the relevant intermediate coupling regime, where formation of JT polaron resonances is a borderline proposition to begin with, the effective potential has only one high-lying configuration ($S = 0$), just as for H_A. This latter case is fully analogous to H_A, with the important exception that the cut-off for pseudo spin-flip scattering is given by $\hbar\omega_o$ rather than by D. Thus, in the present case,

$$kT_K \simeq \hbar\omega_o \cdot \exp(-1/|N(0)J|) \quad (10)$$

where it can be shown that $J \simeq -4V^2/C$.

Based on this result, we predict that a resistivity study of a suitable Vb hydride will reveal a logarithmic Kondo anomaly in the temperature range 0-300K. By "suitable," we mean that the dilute α-phase must be maintained over the relevant range. (Ordered hydride phases are not expected to show the anomaly.) Moreover, since the psuedo-spin operator does not couple to a magnetic field, we expect a <u>nonmagnetic</u> Kondo effect. This clearly distinguishes a JT Kondo effect from the traditional one. Turning the argument around, we propose that any dilute-phase hydride showing a hydrogen-related nonmagnetic Kondo effect provides evidence for hydrogen-stablized JT polaron resonances.

References

I. Low temperature research

1. Mound Activities in Chemical and Physical Research: January-June 1982, MLM-2998 (October 25, 1982), pp. 6-17.

2. O. A. Schaeffer and S. O. Thompson, Rad. Res., 10, 671 (1959).

3. P. C. Souers, E. M. Fearon and R. T. Tsugawa, Cryogenics, 21, 667 (1981).

4. G. T. McConville and D. White, Physica B+C, 107, 271 (1981).

5. G. T. McConville and D. A. Menke, Temperature, Its Measurement and Control in Science and Industry, Vol. 5, 143 (1982).

6. R. C. Kemp, Temperature, Its Measurement and Control in Science and Industry, Vol. 5, 249 (1982).

II. Separation research

1. Mound Facility Activities in Chemical and Physical Research: January-June 1981, MLM-2884 (December 15, 1981), p. 15.

2. Mound Facility Activities in Chemical and Physical Research: January-June 1977, MLM-2450 (October 4, 1977), p. 40.

3. Mound Activities in Chemical and Physical Research: January-June 1982, MLM-2998 (October 25, 1982), p. 25.

4. R. Dawson, F. Khoury and R. Kobayashi, AIChE Journal, 16, 725, 1970.

5. D. T. Jamieson, J. B. Irving and J. S. Tudhope, Liquid Thermal Conductivity, Her Majesty's Stationary Office, Edinburgh, 1975.

6. Y. S. Toloukian, S. C. Saxena and P. Hestermans, Thermophysical Properties of Matter, Vols. 3 and 11, IFI/Plenum, New York, 1975.

7. Mound Activities in Chemical and Physical Research: January-June 1982, MLM-2998 (October 25, 1982), p. 25.

8. Mound Facility Activities in Chemical and Physical Research: July-December 1981, MLM-2892 (May 3, 1982), p. 18.

9. W. M. Rutherford and K. W. Laughlin, Science, 211, 1054 (1981).

10. Mound Facility Activities in Chemical and Physical Research: July-December 1981, MLM-2892, (May 3, 1982), p. 14.

11. Mound Facility Activities in Chemical and Physical Research: January-June 1981, MLM-2884 (December 15, 1981), p. 28.

12. J. D. Lamb, R. M. Izatt, J. J. Christensen and D. J. Eatough, "Thermodynamics and Kinetics of Cation-Macrocycle Interaction," Coordination Chemistry of Macrocyclic Compounds, G. A. Melson (ed.), Plenum Press, New York and London, 1979, pp. 187,198.

13. B. E. Jepson and G. A. Cairns, "Lithium Isotope Effects in Chemical Exchange with (211) Cyrptand," MLM-2622 (June 8, 1979).

14. Mound Facility Activities in Chemical and Physical Research: July-December 1979, MLM-2727 (June 18, 1980), p. 43.

15. W. R. Shields, "Analytical Mass Spectrometry Section: Instrumentation and Procedure of Commerce, National Bureau of Standards, Washington, D.C. (July 1966), p. 41.

16. J. C. Slattery, Momentum Energy and Mass Transfer in Continua, McGraw-Hill, New York (1972).

17. L. Lapidus and N. R. Amundson, J. Phys. Chem., 56, 984 (1952).

18. J. J. van Deemter, F. J. Zuiderweg and A. Klinkenberg, Chem. Eng. Sci. 5, 271 (1956).

19. M. J. Stern, L. N. Kauder and W. Spindel, J. Chem. Phys., 34, 3333 (1961) and J. Chem. Phys., 36, 764 (1962).

20. G. L. Silver, Plutonium Adsorption by Selected Inorganic Compounds, MLM-2692 (October 10, 1980), 42 pp.

21. N. P. Nies and G. W. Campbell, in Boron, Metallo-Boron Compounds, and Boranes, R. M. Adams (ed.), Interscience Publishers, New York, 1964, p. 184.

22. D. Ashboren (Araten), Israel J. Chem., 12, 4, 831 (1974).

23. J. Mellor, A Comprehensive Treatise on Inorganic and Theoretical Chemistry, Vol. V, Longmans, Green and Co., London, 1946, p. 147.

24. H. Remy, Treatise on Inorganic Chemistry, Elsevier Publishing Co., Amsterdam, 1956, p. 342.

25. H. J. Becher, Handbook of Preparative Inorganic Chemistry, G. Brauer (ed.), Academic Press, New York, 1963, p. 796.

III. Metal hydride studies

1. G. C. Abell, Phys. Rev. B, 20, 4773 (1979).

2. G. C. Abell, Phys. Rev. B., 22, 2014 (1980).

3. P. W. Anderson, Phys. Rev., 124, 41 (1961).

4. J. R. Schrieffer and P. A. Wolff, Phys. Rev., 149, 491 (1966); J. R. Schrieffer, J. Appl. Phys., 38, 1143 (1967).

5. J. M. Ziman, "Principles of the Theory of Solids," 2nd Ed., (London: Cambridge Press, 1972).

6. H. R. Krishna-murthy, K. G. Wilson and J. R. Wilkins, Phys. Rev. Lett., 35, 1101 (1975).

7. G. C. Abell, J. Phys. F, 12, 1143 (1982).

8. G. Rickayzen, "Theory of Superconductivity," (New York: Interscience, 1965), Ch. 3.

Distribution

EXTERNAL

TIC-4500, UC-4 and UC-22 (194)

J. R. Blair, DOE/Office of Health and Environmental Research

J. Burnett, DOE/Office of Basic Energy Sciences

K. Gschneidner, Iowa University, Ames, Iowa

N. Haberman, DOE/Division of Nuclear Energy

H. N Hill, DOE/Dayton Area Office

J. N. Maddox, DOE/Office of Health and Environmental Research

L. R. Morss, Argonne National Laboratory

H. A. Schneiderman, Monsanto, St. Louis

F. D. Stevenson, DOE/Office of Basic Energy Sciences

L. Thompson, University of Minnesota

E. L. Venturini, Sandia National Laboratories, Albuquerque

D. White, University of Pennsylvania

H. L. Williams, Monsanto, St. Louis

Monsanto Reports Library, R2C, St. Louis

INTERNAL

G. C. Abell

W. R. Amos

L. R. Baird

R. C. Bowman

D. Cain

R. E. Ellefson

H. N. Friedlander

C. W. Huntington

B. E. Jepson

B. R. Kokenge

G. T. McConville

D. A. Menke

E. D. Michaels

R. H. Nimitz

W. M. Rutherford

G. C. Shockey

G. L. Silver

W. L. Taylor

R. J. Tomasoski

R. E. Vallee

C. J. Wiedenheft

W. R. Wilkes

R. W. York

Document Control

Library (15)

Publications

Published by Information Services

Stephen L. Nowka, Editor